



ELSEVIER

Available online at [www.sciencedirect.com](http://www.sciencedirect.com)

SCIENCE @ DIRECT®

Nuclear Instruments and Methods in Physics Research A 536 (2005) 79–122

NUCLEAR  
INSTRUMENTS  
& METHODS  
IN PHYSICS  
RESEARCH  
Section A

[www.elsevier.com/locate/nima](http://www.elsevier.com/locate/nima)

## Technical design and performance of the NEMO 3 detector

R. Arnold<sup>a</sup>, C. Augier<sup>b,\*</sup>, A.M. Bakalyarov<sup>c</sup>, J. Baker<sup>d</sup>, A. Barabash<sup>e</sup>,  
Ph. Bernaudin<sup>b</sup>, M. Bouchel<sup>b</sup>, V. Brudanin<sup>f</sup>, A.J. Caffrey<sup>d</sup>, J. Cailleret<sup>a</sup>,  
J.E. Campagne<sup>b</sup>, D. Dassié<sup>g</sup>, V. Egorov<sup>f</sup>, K. Errahmane<sup>b</sup>, A.I. Etievre<sup>b</sup>,  
T. Filipova<sup>f</sup>, J. Forget<sup>b</sup>, A. Guiral<sup>g</sup>, P. Guiral<sup>g</sup>, J.L. Guyonnet<sup>a</sup>, F. Hubert<sup>g</sup>,  
Ph. Hubert<sup>g</sup>, B. Humbert<sup>a</sup>, R. Igersheim<sup>a</sup>, P. Imbert<sup>b</sup>, C. Jollet<sup>a</sup>, S. Jullian<sup>b</sup>,  
I. Kisel<sup>f</sup>, A. Klimenko<sup>h</sup>, O. Kochetov<sup>f</sup>, V. Kovalenko<sup>f</sup>, D. Lalanne<sup>b</sup>,  
F. Laplanche<sup>b</sup>, B. Lavigne<sup>b</sup>, V.I. Lebedev<sup>c</sup>, J. Lebris<sup>i</sup>, F. Leccia<sup>g</sup>, A. Leconte<sup>j</sup>,  
I. Linck<sup>a</sup>, C. Longuemare<sup>j</sup>, Ch. Marquet<sup>g</sup>, G. Martin-Chassard<sup>b</sup>, F. Mauger<sup>j</sup>,  
I. Nemchenok<sup>f</sup>, I. Nikolic-Audit<sup>g</sup>, H. Ohsumi<sup>k</sup>, S. Pécourt<sup>b</sup>, F. Piquemal<sup>g</sup>,  
J.L. Reyss<sup>l</sup>, A. Richard<sup>i</sup>, C.L. Riddle<sup>d</sup>, J. Rypko<sup>b</sup>, X. Sarazin<sup>b</sup>, L. Simard<sup>b</sup>,  
F. Scheibling<sup>a</sup>, Yu. Shitov<sup>f</sup>, A. Smolnikov<sup>h</sup>, I. Štekl<sup>m</sup>, C.S. Sutton<sup>n</sup>, G. Szklarz<sup>b</sup>,  
V. Timkin<sup>f</sup>, V. Tretyak<sup>f</sup>, V. Umatov<sup>e</sup>, L. Vála<sup>b,m</sup>, I. Vanushin<sup>e</sup>, S. Vasiliev<sup>h</sup>,  
V. Vasilyev<sup>e</sup>, V. Vorobel<sup>o</sup>, Ts. Vylov<sup>f</sup>, J. Wurtz<sup>a</sup>, S.V. Zhukov<sup>c</sup>

<sup>a</sup>*IReS, IN2P3-CNRS et Université Louis Pasteur, 67037 Strasbourg, France*

<sup>b</sup>*LAL, IN2P3-CNRS et Université de Paris-Sud, 91405 Orsay, France*

<sup>c</sup>*RRC "Kurchatov Institute", 123182 Moscow, Russia*

<sup>d</sup>*INEEL, Idaho Falls, ID 83415, USA*

<sup>e</sup>*ITEP, 117259 Moscow, Russia*

<sup>f</sup>*JINR, 141980 Dubna, Russia*

<sup>g</sup>*CENBG, IN2P3-CNRS et Université de Bordeaux I, 33170 Gradignan, France*

<sup>h</sup>*INR RAS, 117312 Moscow, Russia*

<sup>i</sup>*IPN, IN2P3-CNRS et Université de Paris-Sud, 91405 Orsay, France*

<sup>j</sup>*LPC, IN2P3-CNRS et Université de Caen, 14032 Caen, France*

<sup>k</sup>*Saga University, Saga 840-8502, Japan*

<sup>l</sup>*LSCE, CNRS, 91190 Gif-sur-Yvette, France*

<sup>m</sup>*CTU, Prague, Czech Republic*

<sup>n</sup>*MHC, South Hadley, Massachusetts 01075, USA*

<sup>o</sup>*Charles University, Prague, Czech Republic*

Received 16 June 2004

Available online 20 August 2004

\*Corresponding author.

E-mail address: [augier@lal.in2p3.fr](mailto:augier@lal.in2p3.fr) (C. Augier).

## Abstract

The development of the Neutrino Ettore Majorana Observatory (NEMO~ 3) detector, which is now running in the Fréjus Underground Laboratory (L.S.M. Laboratoire Souterrain de Modane), was begun more than ten years ago. The NEMO 3 detector uses a tracking-calorimeter technique in order to investigate double beta decay processes for several isotopes. The technical description of the detector is followed by the presentation of its performance.

© 2004 Elsevier B.V. All rights reserved.

PACS: 23.40.–s; 14.60.Pq

Keywords: NEMO; Double beta decay; Neutrino; Majorana; Tracking detector; Calorimeter

## 1. Introduction

### 1.1. Objective of the experiment

The primary objective of the Neutrino Ettore Majorana Observatory (NEMO~ 3) experiment is to search for neutrinoless double beta decay for several isotopes. This research is one of the most pressing topics in neutrino physics, for which there is the fundamental problem of whether or not neutrinos are massless. If double beta decay without neutrino emission,  $\beta\beta 0\nu$ , is observed the neutrino can be a massive Majorana particle, which is its own antiparticle.

It was proposed years ago [1] that there could be an exchange of neutrinos between two neutrons in the same nucleus leading to the emission of two electrons and no neutrinos. The Majorana mass term enables such a transition through a  $V-A$  interaction. The observation of the  $\beta\beta 0\nu$  process would then prove the Majorana nature of the neutrino.

It is also possible to investigate  $\beta\beta 0\nu$  transitions to the  $2^+$  excited state, which involves a Majorana mass term through the  $V+A$  interaction. Other mechanisms may contribute to the  $\beta\beta 0\nu$  process, in particular the emission of a Majoron  $M^0$ , the boson associated with spontaneous symmetry breaking of lepton number. The search for the  $\beta\beta M^0$  process involves a three body decay spectrum with the Majoron avoiding detection, which imposes additional constraints on the design of the detector. The objective of the NEMO 3 experiment is to investigate these three decay

modes to further the understanding of double beta decay.

In all double beta decays, which are second-order weak interactions, nuclei decay into daughter nuclei by emitting two electrons accompanied by two undetected neutrinos. This is the  $\beta\beta 2\nu$  process which has already been observed for 10 isotopes:  $^{48}\text{Ca}$ ,  $^{76}\text{Ge}$ ,  $^{82}\text{Se}$ ,  $^{96}\text{Zr}$ ,  $^{100}\text{Mo}$ ,  $^{116}\text{Cd}$ ,  $^{128}\text{Te}$ ,  $^{130}\text{Te}$ ,  $^{150}\text{Nd}$  and  $^{238}\text{U}$  (see Ref. [2] for a review article).

The NEMO 3 experiment aims to search for the effective Majorana neutrino down to a mass  $\langle m_\nu \rangle$  at the level of 0.1 eV. If only a limit is reached on the  $\beta\beta 0\nu$  half-life, an upper limit on  $\langle m_\nu \rangle$  can be inferred from the relation

$$(T_{1/2}^{0\nu})^{-1} = (\langle m_\nu \rangle / m_e)^2 \times |M_{0\nu}|^2 \times G_{0\nu} \quad (1)$$

where  $G_{0\nu}$  is the phase-space factor that is analytically calculated and proportional to the transition energy to the fifth power,  $Q_{\beta\beta}^5$ .  $M_{0\nu}$  is the nuclear matrix element of the relevant isotope for which calculations have large theoretical uncertainties. Given the uncertainty in  $M_{0\nu}$ , a mass limit of 0.1 eV corresponds to a neutrinoless double beta decay with a half-life limit of the order of  $10^{25}$  years for  $^{100}\text{Mo}$ . To improve the sensitivity of a double beta decay experiment it is preferable to study an isotope with a large  $Q_{\beta\beta}$ , not only to get a larger  $G_{0\nu}$ , but also to reduce the background in the search for a  $\beta\beta 0\nu$  signal.

Measurements of a half-life as long as  $10^{25}$  years is challenging. It requires a solid understanding of natural and cosmogenic radioactive backgrounds

in the materials from which the detector is made and backgrounds induced by the radioactivity from the walls and atmosphere in the underground laboratory. Two prototypes, NEMO 1 [3] and NEMO 2 [4], were constructed and run to demonstrate the feasibility of the experimental technique. The development of NEMO 3 was begun more than 10 years ago [5]. It reflects a more than 10-fold enhancement on the NEMO 2 sensitivity in order to measure the double beta decay half-life limits of  $10^{25}$  years for the  $\beta\beta 0\nu$  process,  $10^{23}$  years for the  $\beta\beta M^0$  process, and  $10^{22}$  years for the  $\beta\beta 2\nu$  process.

### 1.2. General description of the NEMO 3 detector

The philosophy behind NEMO 3 is the direct detection of the two electrons from  $\beta\beta$  decay by a tracking device and a calorimeter. The NEMO 3 detector, for which the general layout is shown in Fig. 1, is similar in function to the earlier prototype detector, NEMO 2, but has lower

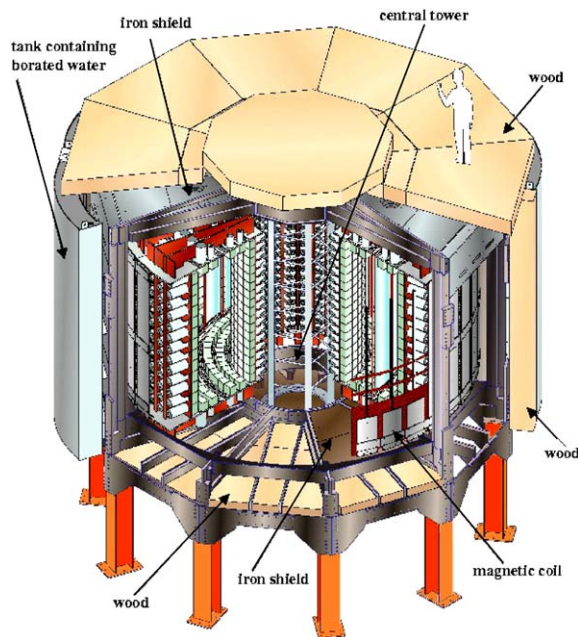


Fig. 1. An exploded view of the NEMO 3 detector. Note the coil, iron  $\gamma$ -ray shield, and the two different types of neutron shields, composed of water tanks and wood. The paraffin shield under the central tower is not shown on the picture.



Fig. 2. View of the NEMO 3 detector in the LSM before the installation of the last sector.

radioactivity and is able to accommodate up to 10 kg of double beta decay isotopes.

The NEMO 3 detector is now installed in the Fréjus Underground Laboratory (LSM)<sup>1</sup> in France. It is cylindrical in design and divided into 20 equal sectors, as shown in Figs. 2 and 3. The segmentation permits easy access to a patchwork of source foils of the different isotopes. This patchwork is also cylindrical in form. It is 3.1 m in diameter, 2.5 m in height and 30–60 mg/cm<sup>2</sup> thick.

The source foils are fixed vertically between two concentric cylindrical tracking volumes composed of 6180 open octagonal drift cells. The drift cells are 270 cm long, operating in Geiger mode at 7 mbar above atmospheric pressure, with a partial pressure of 40 mbar of ethyl alcohol in a mixture with helium gas. The cells run vertically and three-dimensional tracking is accomplished with the arrival time of the signals on the anode wires and

<sup>1</sup>Laboratoire Souterrain de Modane.

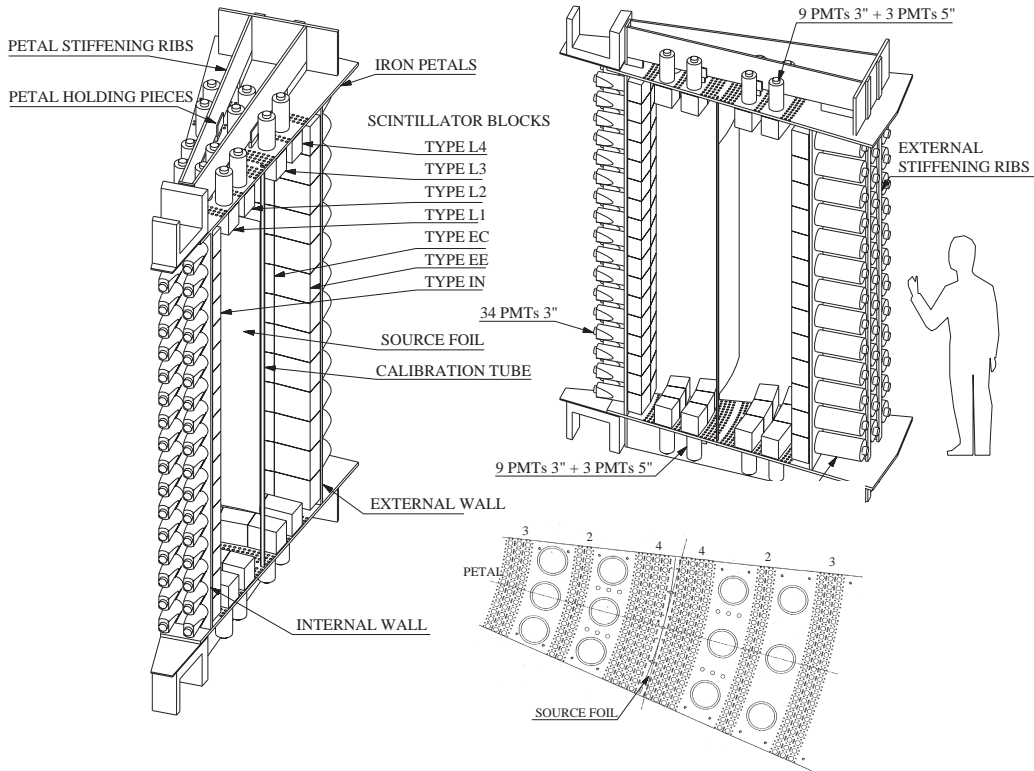


Fig. 3. One sector of NEMO 3 with details on the source foil, scintillator blocks and photomultipliers. The Geiger cells are located between the internal and external walls. L4, L3,... IN identify different shapes of scintillator blocks. A petal (end-cap) is also shown with the “4-2-3” layer configuration for the Geiger cells.

the plasma propagation times to the ends of the drift cells.

Energy and time-of-flight measurements are acquired from plastic scintillators covering the two vertical surfaces of the active tracking volume. To further enhance the acceptance efficiency, the end-caps (the top and bottom of the detector) are also equipped with scintillators in the spaces between the drift cell layers. This calorimeter is made of 1940 large blocks of scintillators coupled to very low radioactivity 3” or 5” photomultiplier tubes (PMTs). The 10 cm thick blocks of scintillator yield a high photon detection efficiency. Fig. 4 shows a picture of one sector of the NEMO 3 detector.

A solenoid surrounding the detector produces a 25 G magnetic field parallel to the foil axis, in order to identify the particle charge. Pairs ( $e^+e^-$ ) are produced in the source foils in the 1–10 MeV

region by high-energy  $\gamma$ -rays from neutron capture. The curvature measurements also permit an efficient rejection of incoming electrons.

Finally, an external shield, in the form of 20 cm of low radioactivity iron, covers the detector to reduce  $\gamma$ -rays and thermal neutrons. Outside of this iron there is a borated water shield to thermalize fast neutrons and capture thermal neutrons.

In the NEMO 3 detector, electrons, positrons, photons and  $\alpha$ -particles can be identified. Thus, the detector is able to detect multi-particle events in the low energy domain of natural radioactivity.

### 1.3. Background of the experiment

The most significant concern in this double beta decay experiment is the background. The calorimeter measures the energy of the two electrons

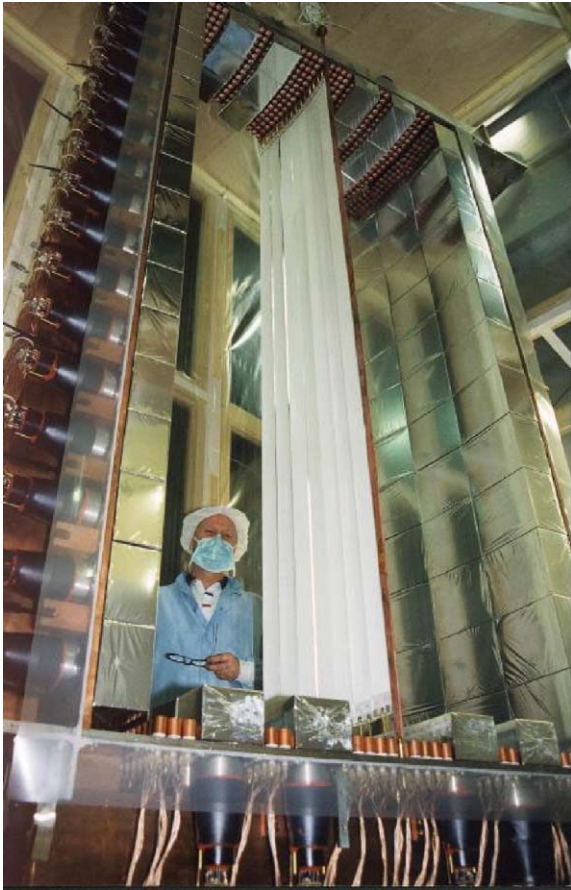


Fig. 4. View of the third sector in the source mounting room just after the installation of the tellurium source.

emitted from a common vertex in the source foil. The energy region of interest for the  $\beta\beta 0\nu$  signal is around 3 MeV ( $Q_{\beta\beta}(^{100}\text{Mo}) = 3.034$  MeV and  $Q_{\beta\beta}(^{82}\text{Se}) = 2.995$  MeV [6]). This energy region is shared by some energetic natural radioactivity, which can produce two electrons in the source which mimic  $\beta\beta 0\nu$  decays. The key to the success of the experiment is to be able to positively identify these background events with high efficiency.

### 1.3.1. Natural radioactivity decay chains and other radioactive isotopes

In general, natural radioactivity coming from very long half-life isotopes such as potassium (K), uranium (U) and thorium (Th) needs to be

carefully monitored. The decay chain for  $^{235}\text{U}$  is not taken into account, because even though the half-life is  $7.04 \times 10^8$  years its natural isotopic abundance is only 0.7% and its decay chain daughter nuclei do not generate enough energy to mimic the  $\beta\beta 0\nu$  signal. Concerning  $^{40}\text{K}$ , the energy range of these decays is again not a background concern for the  $\beta\beta 0\nu$ 's signal.

From the natural decay chains of  $^{238}\text{U}$  and  $^{232}\text{Th}$ , only  $^{214}\text{Bi}$  and  $^{208}\text{Tl}$  are  $\beta$ -decay isotopes with  $Q_{\beta}$  greater than 3 MeV (with respective  $Q_{\beta}$  values of 3.270 and 4.992 MeV, and respective half-lives of 19.9 and 3.05 min [7]). Thus,  $^{214}\text{Bi}$  and  $^{208}\text{Tl}$  produce  $\gamma$ -rays and electrons that are energetic enough to simulate  $\beta\beta 0\nu$  events at 3 MeV (energies and intensities of  $\gamma$ -rays from natural radioactivity decay chains of  $^{238}\text{U}$  and  $^{232}\text{Th}$  can be found in Ref. [8]). The most energetic  $\gamma$ -rays are from  $^{208}\text{Tl}$  (2.615 MeV) for which the branching ratio is 36%.

Radon ( $^{222}\text{Rn}$ ,  $T_{1/2} = 3.824$  days) and thoron ( $^{220}\text{Rn}$ ,  $T_{1/2} = 55.6$  s) are  $\alpha$ -decay isotopes, which have  $^{214}\text{Bi}$  and  $^{208}\text{Tl}$  as daughter isotopes, respectively. Coming mainly from the rocks and present in the air, the  $^{222}\text{Rn}$  and  $^{220}\text{Rn}$  are very diffusion prone rare gases which can enter the detector. Subsequent  $\alpha$ -decays of these gases give  $^{218}\text{Po}$  and  $^{216}\text{Po}$ , respectively, which can contaminate the interior of the detector.

In the Bi–Po process,  $^{214}\text{Bi}$  has  $^{214}\text{Po}$  as its daughter isotope which emits  $\alpha$ -particles with a 164  $\mu\text{s}$  half-life. Electronics designed to see delayed tracks for up to 710  $\mu\text{s}$  tag these  $\alpha$ -particles in order to measure and reject the  $^{214}\text{Bi}$  and  $^{222}\text{Rn}$  backgrounds (see Section 2.4.2).

### 1.3.2. External and internal backgrounds

When describing the background, it is convenient to distinguish between the “internal” and “external” sources. The internal backgrounds come from radioactive contaminants inside the  $\beta\beta$  source foil, while external backgrounds come from radioactive contaminants outside the  $\beta\beta$  source foils, which interact with the detector.

The internal background for the  $\beta\beta 0\nu$  signal in the 3 MeV region has two origins. The first is the tail of the  $\beta\beta 2\nu$  decay distribution of the source, which cannot be separated from the  $\beta\beta 0\nu$  signal

and the level of overlap depends on the energy resolution of the detector. Thus, this ultimately defines the half-life limits to which  $\beta\beta_{0\nu}$  can be searched for. The second background comes from the  $\beta$ -decays of  $^{214}\text{Bi}$  and  $^{208}\text{Tl}$ , which are present in the source at some level. They can mimic  $\beta\beta$  events by three mechanisms. These are  $\beta$ -decay accompanied by an electron conversion process, Möller scattering of  $\beta$ -decay electrons in the source foil and  $\beta$ -decay emission to an excited state followed by a Compton scattered  $\gamma$ -ray. The last mechanism can be detected as two electron events if the  $\gamma$ -ray is not detected. Thus, the experiment requires ultra-pure source foils. The maximum levels of impurities in the source have been calculated so as to produce fewer events than the tail of the  $\beta\beta_{2\nu}$  decay gives in the region of interest for  $\beta\beta_{0\nu}$ .

The external background is defined as events produced by  $\gamma$ -ray sources located outside the source foils and interacting with them. The interaction of  $\gamma$ -rays in the foils can lead to two electron-like events by  $e^+e^-$  pair creation, double Compton scattering or Compton followed by Möller scattering. One of the main sources of this external radioactivity comes from the PMTs, but there are other sources too, such as cosmic rays, radon and neutrons. To decrease the background for the NEMO 3 detector it was placed at a depth of 4800 m water equivalent, where cosmic ray fluxes have been found to be negligible. Two shields and a magnetic field suppress the backgrounds from  $\gamma$ -rays and neutrons. The vigorous air ventilation system in the laboratory reduces radon levels down to 10–20 Bq/m<sup>3</sup>. All the materials used in the detector have been selected for their radiopurity properties and in particular, a substantial effort has been made to reduce the contamination of the PMTs from  $^{40}\text{K}$ ,  $^{214}\text{Bi}$  and  $^{208}\text{Tl}$  (see Sections 2.2.3 and 2.8).

Consequently, in the construction of the NEMO 3 experiment every attempt has been made to minimize internal and external backgrounds by purification of the enriched isotope samples and by carefully selecting all the detector materials. As it was shown with the NEMO 2 prototype, the NEMO 3 detector will be able to characterize and measure its own background.

## 2. Technical design of the NEMO 3 detector

### 2.1. The NEMO 3 sources

#### 2.1.1. Introduction

The primary design feature of the NEMO 3 experiment was to have the detector and the source of the double beta decay independent, unlike the case of the  $^{76}\text{Ge}$  experiments. This permits one to study several double beta decay isotopes, a critical point is to be able to confirm an excess of  $\beta\beta_{0\nu}$  events from one isotope with another isotope. It also reduces the dependence of the interpretation of the result on the nuclear matrix elements. Furthermore, a rich study of the backgrounds and systematic effects is possible.

The choice of which nuclei to study was affected by several parameters. These include the transition energy ( $Q_{\beta\beta}$ ), the nuclear matrix elements ( $M_{0\nu}$  and  $M_{2\nu}$ ) of the transitions for  $\beta\beta_{0\nu}$  and  $\beta\beta_{2\nu}$  decays, the background in the energy region surrounding the  $Q_{\beta\beta}$  value, the possibility of reducing the radioactivity of the isotope studied to acceptable levels, and finally the natural isotopic abundance of the candidate. Basing the choice singularly on  $M_{0\nu}$  is not advisable because the calculations are too uncertain. A good criterion for isotope selection is the  $Q_{\beta\beta}$  value with respect to backgrounds. As explained in Section 1.3, the 2.615 MeV  $\gamma$ -ray produced in the decay of  $^{208}\text{Tl}$  is consistently a troublesome source of background and it is important to select  $\beta\beta$  candidates with a  $Q_{\beta\beta}$  value above this transition. The natural isotopic abundance is another useful criterion because in general the higher the abundance the easier the enrichment process. Typically only isotopic abundances greater than 2% were considered. Five nuclei satisfy these two criteria:  $^{116}\text{Cd}$ ,  $^{82}\text{Se}$ ,  $^{100}\text{Mo}$ ,  $^{96}\text{Zr}$  and  $^{150}\text{Nd}$  (with respective  $Q_{\beta\beta}$  values of 2804.7, 2995.2, 3034.8, 3350.0 and 3367.1 keV and respective isotope abundance values of 7.5%, 9.2%, 9.6%, 2.8% and 5.6% [6]). Given this list and the availability of  $^{100}\text{Mo}$ , much effort has been focused by the NEMO collaboration on this isotope (it had already been studied by the NEMO 2 prototype [9]). However the focus is not exclusively on  $^{100}\text{Mo}$ ,

in view of the fact that the detector can house several different sources.

There have been improvements in the isotopic enrichment processing in Russia, where all the double beta decay sources were produced. Thus the  $^{48}\text{Ca}$  isotope has been added to the list of interesting sources. Note that  $^{48}\text{Ca}$  fails to meet the abundance selection criterion but has an impressive  $Q_{\beta\beta}$  value ( $Q_{\beta\beta} = 4272.0\text{ keV}$  and isotope abundance of 0.187% [6]). Finally,  $^{130}\text{Te}$  (with  $Q_{\beta\beta}$  value of 2528.9 keV and isotope abundance of 33.8% [6]) has been added for  $\beta\beta 2\nu$  studies. Historically,  $^{130}\text{Te}$  has had two different geochemical half-life measurements [10,11], which are inconsistent with each other and a reliable one is sought here.

A description of the current population of the 20 sectors of NEMO 3 follows. To study the  $\beta\beta 0\nu$  processes 6914 g of  $^{100}\text{Mo}$  and 932 g of  $^{82}\text{Se}$  are housed in twelve and two sectors, respectively. The objective here is to reach a sensitivity for the effective neutrino mass on the order of 0.1 eV. Several other  $\beta\beta$  decay isotopes in smaller quantities have been introduced to study the  $\beta\beta 2\nu$  processes which will complement the very

detailed studies provided by the  $^{100}\text{Mo}$  and  $^{82}\text{Se}$  on angular distributions and single electron energy spectra. This second tier of isotope samples consists of 454 g of  $^{130}\text{Te}$  (2 sectors), 405 g of  $^{116}\text{Cd}$  (1 sector), 37 g of  $^{150}\text{Nd}$ , 9 g of  $^{96}\text{Zr}$  and 7 g of  $^{48}\text{Ca}$ . Finally, source foils with high levels of radiopurity, which are effectively void of internal backgrounds, will measure the external background in the experiment. This not only accounts for the presence of 621 g of copper but also a very pure oxide of natural tellurium, which permits one to study the background near 3 MeV. This natural tellurium also provides an investigation of the  $\beta\beta 2\nu$  because the natural abundance of isotope 130 for tellurium is 33.8%, which gives 166 g of  $^{130}\text{Te}$ .

For each sector, a source frame was constructed on which were placed seven strips. The mean length of the strips is 2480 mm with a width of 63 mm if they are on the edges of the frame or 65 mm for the five strips in the middle of the frame. All the strips are attached to the frames in a clean room at the LSM where they are then introduced into the sectors. The so-called “NEMO 3 camembert” depicts the distribution of the sources in the 20 sectors, Fig. 5.

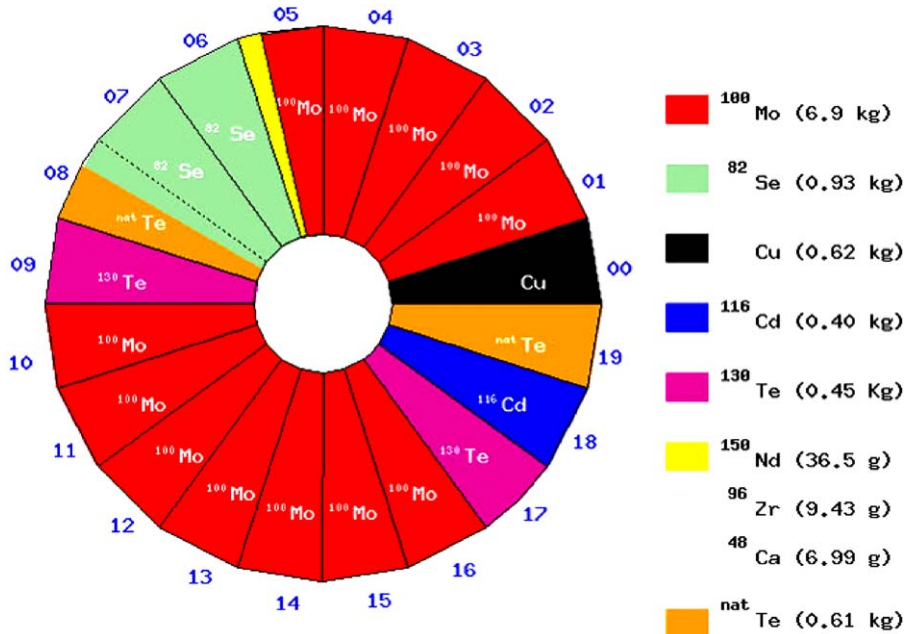


Fig. 5. The source distribution in the 20 sectors of NEMO 3.

The thickness of the source foils was chosen to take into account the energy resolution, which is fixed by the calorimeter design. The detector efficiency for the  $\beta\beta_{0\nu}$  process is not compromised as long as the surface densities of the foils do not exceed  $60 \text{ mg/cm}^2$ . As a consequence the source foils have surface densities between  $30$  and  $60 \text{ mg/cm}^2$ , which means a thickness lower than  $60 \mu\text{m}$  for the metallic foils (density of  $\sim 10 \text{ g/cm}^3$ ) and lower than  $300 \mu\text{m}$  for composite foils (density of  $\sim 2 \text{ g/cm}^3$ ).

As indicated above, NEMO 3 sources are metallic or composite. Cadmium, copper and a fraction of the molybdenum foils are metallic sources. Composite foils are a mixture of source powder and organic glue. For the  $^{100}\text{Mo}$  64% are in the form of composite strips. The selenium, tellurium, zirconium, neodymium and calcium foils are all composite foils.

For composite foils, the glue is made from water and some percentage of polyvinyl alcohol (PVA). This mixture is laid down on a Mylar sheet and then covered by another sheet forming a sandwich-like structure. These sheets are often referred to as backing films, which provide mechanical rigidity. The Mylar sheets have undergone a special processing in which a large number of microscopic holes (around  $0.4 \mu\text{m}$  in diameter) have been created to insure a good bond with the glue. There are three types of backing film used in the experiment. Type 1 has a thickness of  $18 \mu\text{m}$  and around  $7 \times 10^7$  holes/ $\text{cm}^2$ . Type 2 has a thickness of  $19 \mu\text{m}$  and around  $2 \times 10^7$  holes/ $\text{cm}^2$ . Type 3, which is  $23 \mu\text{m}$  thick, has around  $7 \times 10^7$  holes/ $\text{cm}^2$ . The holes were made first by irradiating the Mylar at JINR with a  $^{84}\text{Kr}$  ion beam of  $3 \text{ MeV/nucleon}$  and a total beam intensity on target of, respectively,  $2.4 \times 10^{10}$  ions/s (for Type 2) and  $8.4 \times 10^{10}$  ions/s (for Type 1 and Type 3 backing films). For each point on the Mylar surface,  $3.6 \times 10^9$  and  $1.3 \times 10^{10}$  ions were incident during an exposure time of  $0.15 \text{ s}$  corresponding to ion track densities in the film of  $2 \times 10^7$  and  $7 \times 10^7$  holes/ $\text{cm}^2$ , respectively. The next step in preparing the film was chemically etching it with  $\text{NaOH}$  ( $5 \text{ M}$ ) at  $70^\circ \text{C}$ , then the film was washed with water and  $1\% \text{ CH}_3\text{COOH}$  (acetic acid) and finally dried with hot air. All the products (Mylar,

water, acid...) used to process the backing film have been selected for their radiopurity with High Purity Germanium (HPGe) detector measurements at the LSM (the HPGe detectors are from Eurisy Mesures Company). The characteristics of all the source foils' strips in the 20 sectors are summarized in Tables 1 and 2.

### 2.1.2. Radiopurity of the sources with respect to $^{214}\text{Bi}$ and $^{208}\text{Tl}$

As presented in Section 1.3, the presence of impurities in the source foils may give rise to two-electron events which mimic  $\beta\beta$  decay and produce background events in the region of the  $\beta\beta_{0\nu}$  signal. These impurities have been sufficiently reduced that given the energy resolution of the calorimeter, the ultimate background for the  $\beta\beta_{0\nu}$  signal is the tail of the  $\beta\beta_{2\nu}$  decay distribution. This is why acceptable levels of  $^{214}\text{Bi}$  and  $^{208}\text{Tl}$  in the foils depends on the number of  $\beta\beta_{2\nu}$  events in the region  $2.8\text{--}3.2 \text{ MeV}$ . For  $10 \text{ kg}$  of  $^{100}\text{Mo}$  ( $Q_{\beta\beta} = 3.035 \text{ MeV}$ ), one background event/year is expected from the  $\beta\beta_{2\nu}$  process above  $2.8 \text{ MeV}$ . As a consequence, the maximum levels of  $^{214}\text{Bi}$  and  $^{208}\text{Tl}$  contamination in the Mo source have been calculated to ensure that  $\beta\beta_{2\nu}$  is the limiting background, that means that  $^{214}\text{Bi}$  and  $^{208}\text{Tl}$  should yield less than  $0.4$  background events/year above  $2.8 \text{ MeV}$  for  $10 \text{ kg}$  of  $^{100}\text{Mo}$ . The associated limits are thus:

$$A_{(^{100}\text{Mo})}(^{214}\text{Bi}) < 0.3 \text{ mBq/kg} \quad (2)$$

$$A_{(^{100}\text{Mo})}(^{208}\text{Tl}) < 0.02 \text{ mBq/kg.} \quad (3)$$

For  $^{82}\text{Se}$  the  $T_{1/2}^{2\nu}$  is 10 times longer than for  $^{100}\text{Mo}$ , however the available mass of this isotope is only  $1 \text{ kg}$ . Similarly, simulations have given the maximum levels of contamination for  $^{214}\text{Bi}$  and  $^{208}\text{Tl}$  in a  $1 \text{ kg}$  Se source foil:

$$A_{(^{82}\text{Se})}(^{214}\text{Bi}) < 0.7 \text{ mBq/kg} \quad (4)$$

$$A_{(^{82}\text{Se})}(^{208}\text{Tl}) < 0.05 \text{ mBq/kg.} \quad (5)$$

No specific limits for activities of these contaminants were required for the other isotopes. Given the low mass of these isotopes, the limits obtained



Table 1  
Characteristics of the source strips for each of the NEMO 3 sectors 00–09

Sector	Source strips	$\eta$ (%)	$M_1$ (g)	$M_2$ (g)	$M_3$ (g)
00	7 of $^{nat}\text{Cu}$ (M)	/	620.8	620.8	620.8 $^{nat}\text{Cu}$
01	5 of $^{enr}\text{Mo}$ (M)	95.14	424.21	423.22	401.76 $^{100}\text{Mo}$
	2 of $^{enr}\text{Mo}$ (C)	95.14	176.22	145.08	137.72 $^{100}\text{Mo}$
02	7 of $^{enr}\text{Mo}$ (M)	1 and 2: 96.81	186.44	186.06	179.76 $^{100}\text{Mo}$
		3 to 7: 98.51	434.88	434.40	426.94 $^{100}\text{Mo}$
03	7 of $^{enr}\text{Mo}$ (M)	98.90	697.32	696.47	686.29 $^{100}\text{Mo}$
04	7 of $^{enr}\text{Mo}$ (M)	97.90	614.63	614.14	600.05 $^{100}\text{Mo}$
05	2 of $^{enr}\text{Mo}$ (M)	1 and 2: 98.20	188.27	187.89	184.14 $^{100}\text{Mo}$
		3 of $^{enr}\text{Mo}$ (C)	3: 96.66	109.22	90.07
		4: 98.20	108.76	90.16	88.34 $^{100}\text{Mo}$
		5: 95.80	87.00	70.85	67.73 $^{100}\text{Mo}$
	1 of $^{enr}\text{Nd}_2\text{O}_3$ (C)	6: 91.0	56.68	40.18	36.55 $^{150}\text{Nd}$
	1/2 of $^{enr}\text{ZrO}_2$ (C)	57.3	11.57	7.15	ITEP: 4.10 $^{96}\text{Zr}$
	(2 parts)	57.3	14.94	9.27	INR: 5.31 $^{96}\text{Zr}$
	1/4 of $^{enr}\text{CaF}_2$ (C)	73.1	18.516	9.572	6.997 $^{48}\text{Ca}$
	1/4 of back. film				
06	7 of $^{enr}\text{Se}$ (C)	97.02	455.67	385.31	373.80 $^{82}\text{Se}$
07	7 of $^{enr}\text{Se}$ (C)	96.82	535.04	460.65	446.03 $^{82}\text{Se}$
08	2 of $^{enr}\text{Se}$ (C)	1: 96.95	73.58	63.24	61.31 $^{82}\text{Se}$
		2: 97.02	62.78	52.82	51.25 $^{82}\text{Se}$
	5 of $^{nat}\text{TeO}_2$ (C)	3 to 7: 33.8	346.44	189.19	63.94 $^{130}\text{Te}$
09	7 of $^{enr}\text{TeO}_2$ (C)	89.4	380.86	255.77	228.61 $^{130}\text{Te}$

$\eta$  is the percentage of  $\beta\beta$  decay isotope in the enriched sample;  $M_1$ ,  $M_2$  and  $M_3$  are, respectively, the total mass of material in the foils, the mass of the investigated element in the foils, and the mass of the relevant  $\beta\beta$  decay isotope in the foils. In this table, (M) and (C) identify the metallic and composite foil.

Table 2  
Characteristics of the source strips for each of the NEMO 3 sectors 10–19

Sector	Source	$\eta$ (%)	$M_1$ (g)	$M_2$ (g)	$M_3$ (g)
10	7 of $^{enr}\text{Mo}$ (C)	1 and 2: 95.14	205.9	170.14	161.51 $^{100}\text{Mo}$
		3 to 6: 96.66	414.68	339.94	327.92 $^{100}\text{Mo}$
11	7 of $^{enr}\text{Mo}$ (C)	7: 96.32	102.91	84.73	81.45 $^{100}\text{Mo}$
		5: 95.14	107.88	89.44	84.92 $^{100}\text{Mo}$
		others: 96.66	614.12	503.73	485.93 $^{100}\text{Mo}$
12	7 of $^{enr}\text{Mo}$ (C)	95.14	728.25	601.59	571.89 $^{100}\text{Mo}$
13	7 of $^{enr}\text{Mo}$ (C)	2 and 4: 98.95	213.73	177.74	175.46 $^{100}\text{Mo}$
		others: 96.20	508.93	420.9	404.1 $^{100}\text{Mo}$
14	7 of $^{enr}\text{Mo}$ (C)	98.95	735.11	608.07	601.00 $^{100}\text{Mo}$
15	7 of $^{enr}\text{Mo}$ (C)	96.20	753.85	627.59	602.62 $^{100}\text{Mo}$
16	7 of $^{enr}\text{Mo}$ (C)	1, 2, 4, 7: 95.14	391.64	318.97	302.79 $^{100}\text{Mo}$
		3 and 5: 96.20	217.74	181.23	174.0 $^{100}\text{Mo}$
		6: 95.30	102.35	84.49	80.34 $^{100}\text{Mo}$
17	7 of $^{enr}\text{TeO}_2$ (C)	89.4	375.52	252.01	225.29 $^{130}\text{Te}$
18	7 of $^{enr}\text{Cd}$ (M)	93.2	491.18	434.42	404.89 $^{116}\text{Cd}$
19	7 of $^{nat}\text{TeO}_2$ (C)	33.8	547.18	301.89	102.04 $^{130}\text{Te}$

$\eta$  is the percentage of  $\beta\beta$  decay isotope in the enriched sample;  $M_1$ ,  $M_2$  and  $M_3$  are, respectively, the total mass of material in the foils, the mass of the investigated element in the foils, and the mass of the  $\beta\beta$  decay isotope in the foils. In this table, (M) and (C) are written, respectively, for metallic and composite foil.

are not expected to be as competitive with the Mo and Se sources.

### 2.1.3. Production and enrichment of molybdenum

The isotopic abundance of  $^{100}\text{Mo}$  is 9.6% in  $^{\text{nat}}\text{Mo}$ . Using enrichment processes in Russia under the control of ITEP, Mo samples with levels of  $95.14 \pm 0.05\%$  to  $98.95 \pm 0.05\%$   $^{100}\text{Mo}$  were produced having a total mass of 10 kg.

The enrichment process involves the production of  $\text{MoF}_6$  gas from natural Mo. This gas then centrifuged to isolate the heavier Mo isotope such as  $^{100}\text{Mo}$ . The next step is an oxidation–reduction reaction on the enriched  $^{100}\text{MoF}_6$  gas which yields  $^{100}\text{MoO}_3$   $^{100}\text{Mo}$  metallic powder.

Radioactivity measurements of this enriched Mo powder have shown that the enrichment process must be complemented with a purification process, more specifically thorium extraction. However the best measurements obtained with the HPGe spectrometer ( $\sim(1-8)\text{mBq/kg}$  for  $^{214}\text{Bi}$  and  $\sim(0.4-2)\text{mBq/kg}$  for  $^{208}\text{Tl}$ ) did not satisfy the specific requirements for NEMO 3 given in Eqs. (2) and (3). To reach these levels, the collaboration decided to investigate two different purification methods in parallel: a physical process and a chemical process. The methods were refined using samples of natural molybdenum. HPGe measurements were made before and after processing to identify improvements in the purification processes.

### 2.1.4. Physical purification of the enriched Mo powder and metallic strip fabrication

Enriched Mo powder is used directly to both purify and produce metallic foils. This purification process, developed by ITEP, involves transforming the powder into an ultrapure monocrystal with a mass of around 1 kg.

The powder is first pressed to obtain a solid Mo sample. Then the Mo is locally melted in a vacuum with an electron beam and a monocrystal is drawn from the liquid portion. Impurities coming from natural radioactivity decay chains make a migration towards the crystal extremities, because these are more soluble in the melting zone than molybdenum. Finally, cutting the skin of impurities off the crystal and repeating the process, one

obtains a very pure sample, from which an enriched purified Mo monocrystal can be grown, with a 20 mm diameter.

“Short” metallic strips, which are between 44 and  $63\mu\text{m}$  thick and between 64 and 1445 mm long, are fabricated from the cut monocrystal by heating and rolling it in a vacuum to avoid pollution. The next step is to trim the edges to obtain short strips 63–65 mm wide. Wastes from each step can be recycled, either by the physical or chemical method.

After the radioactivity measurements (see Table 3 for the “best” limits), three to five short strips are attached end-to-end to create a NEMO 3 strip with a length of around 2500 mm.

Metallic Mo strips were placed in sectors 02, 03 and 04. There are also five additional strips in sector 01 and two strips in sector 05, which give a combined mass of  $(2479 \pm 5)\text{g}$  of  $^{100}\text{Mo}$ .

### 2.1.5. Chemical purification of the enriched Mo powder and fabrication of composite strips

The chemical purification process also starts with the metallic powder. The focus of this method is to remove long lived radioactive isotopes of the  $^{238}\text{U}$  and  $^{232}\text{Th}$  decay chains while filling Ra sites with Ba by spiking the sample during the processing. The process takes advantage of an equilibrium break in the  $^{238}\text{U}$  and  $^{232}\text{Th}$  decay chains, which can selectively transform these chains to non-equilibrium states in which only short lifetime daughters exist. The purification process was carried out in a class 100 clean room at INEEL. It is described in Ref. [12].

Radioactivity measurements of the purified enriched Mo powder samples were made with HPGe spectroscopy in the LSM. The limits,  $A(^{214}\text{Bi}) < 0.2$  and  $A(^{208}\text{Tl}) < 0.05\text{mBq/kg}$ , are the achievable levels for the HPGe detectors. The required limit on  $^{214}\text{Bi}$  (Eq. (2)) is directly measurable. The task of measuring the required limit for  $^{208}\text{Tl}$  (Eq. (3)) is beyond the practical measuring limits of the HPGe detectors in the LSM. However, the chemical extraction factors defined as the ratio of contamination before and after purification were measured [12] for natural and enriched Mo. This study implied by Ra extraction limits and indirectly inferred by

Table 3  
Radioactivity measurements for the NEMO 3 source foils (in mBq/kg)

Source sample activity (mBq/kg)	Meas. mass (g)	Exp. (h)	$^{40}\text{K}$	$^{235}\text{U}$	$^{238}\text{U}$ chain		$^{232}\text{Th}$ chain	
					$^{234}\text{Th}$	$^{214}\text{Pb}$ $^{214}\text{Bi}$	$^{228}\text{Ac}$	$^{208}\text{Tl}$
$^{100}\text{Mo}$ (M)				1.5				
2479 g $^{100}\text{Mo}$ (C)	733	840	<5	$\pm 0.3$	<15	<0.39	<0.5	<0.11
4435 g $^{100}\text{Mo}$ (C)	735	648	<6	<0.3	<15	<0.34	<0.3	<0.10
$^{82}\text{Se}$ (C)	800	628	$\pm 5$	$\pm 0.7$	<18	$\pm 0.5$	<1	$\pm 0.1$
932 g $^{82}\text{Se}$			200	8.5				
	292	500	$\pm 20$	$\pm 0.9$	<25	<4.2	<4	<0.70
$^{130}\text{TeO}_2$ (C)							1.7	
454 g of $^{130}\text{Te}$	633	666	<8	<0.5	<20	<0.67	$\pm 0.7$	<0.46
$^{116}\text{Cd}$	257	778	<13	<0.5	<12	<1.5	<2	<0.5
((M) + mylar)								
405 g of $^{116}\text{Cd}$	299	368	<20	<1	<56	<1.7	<4	<0.83
$^{150}\text{Nd}_2\text{O}_3$ (C)							20	10
37.0 g of $^{150}\text{Nd}$	58.2	458	<70	<1	<66	<3.0	$\pm 7$	$\pm 2$
$^{96}\text{ZrO}_2\text{O}_2$ ITEP (C)								
4.1 g of $^{96}\text{Zr}$	13.7	624	<217	<7	<222	<16	<23	<10
$^{96}\text{ZrO}_2$ INR (C)			583					
5.3 g of $^{96}\text{Zr}$	16.6	456	$\pm 167$	<10	<211	<14	<27	<5.5
$^{48}\text{CaF}_2$ (C)								
6.99 g of $^{48}\text{Ca}$	24.56	1590	<50	<2	<15	<4	<6	<2
$^{\text{nat}}\text{TeO}_2$ (C)			8					
166 g of $^{130}\text{Te}$	620	700	$\pm 3$	<0.3	<17	<0.17	<0.9	<0.090
Cu (M) 621 g	1656	853	<8	<0.2	<5	<0.12	<0.4	<0.040

The total enriched mass of each isotope is given in bold characters. The error bars are statistical uncertainties at the  $1\sigma$  level while the limits are at the  $2\sigma$  level. A systematic uncertainty of about 10% is associated with the Monte-Carlo calculations for the HPGe detector efficiencies. Only the lower limits obtained for  $^{100}\text{Mo}$  are presented, for both metallic and composite strips. In the case of  $^{48}\text{CaF}_2$  the results are for the powder.

measurable quantities of  $^{235}\text{U}$  in the enriched Mo samples, showed that there is strong evidence that the  $^{208}\text{Tl}$  contamination will be below the NEMO 3 design criteria. Ultimately, the NEMO 3 detector will measure this activity.

The chemically purified  $^{100}\text{Mo}$  is used to make composite foils in the method previously discussed. There are two types of backing film used, Type 1 for sector 01 and Type 2 for sectors 05 and 10 through 16.

To produce the composite strips, the first step involves sieving the powder to keep only grains with diameters smaller than  $45\ \mu\text{m}$ . Then, the residual is ground up and several additional sieving processes are undertaken so the grains are

small enough to ensure a good bond to the backing foil. Next the powder is mixed with the glue (water and PVA). The mixture is introduced into a syringe, which is heated with ultra-sound to obtain a paste. This paste of desired thickness is uniformly spread onto one of the two Mylar foils (backing film). After 10 h of drying, the composite strip is cut to length with a surface density lower than  $60\ \text{mg}/\text{cm}^2$ . The total mass of  $^{100}\text{Mo}$  in composite foils is  $(4435 \pm 22)\ \text{g}$ .

#### 2.1.6. Production, enrichment and purification processes for other isotopes

- $^{82}\text{Se}$  source

There is sufficient mass of  $^{82}\text{Se}$  to study the  $\beta\beta 0\nu$  process. One can use a similar enrichment process to produce  $^{82}\text{SeF}_6$  gas as that used for the Mo. The next step is an electrical discharge in the gas to obtain the enriched Se powder.

Two different production runs of 500 g for  $^{82}\text{Se}$  powder were carried out. They had an enrichment factor of  $97.02 \pm 0.05\%$  for run 1 and  $96.82 \pm 0.05\%$  for run 2. No subsequent purification process was carried out. A portion of run 1 was already used in the NEMO 2 prototype and a value for the  $^{214}\text{Bi}$  contamination was measured, but the contaminants were found to be concentrated in small “hot spots” and rejected in the analysis via identification of the vertex of the candidate events [13]. The  $^{82}\text{Se}$  used in NEMO 2 foils was recovered and used to produce composite strips for NEMO 3. The sample of material from run 2 plus the remaining part of run 1 were also used to produce composite strips. Low activities in  $^{214}\text{Bi}$  ( $1.2 \pm 0.5$  mBq/kg) and  $^{208}\text{Tl}$  ( $0.4 \pm 0.1$  mBq/kg) were measured for 0.8 kg of  $^{82}\text{Se}$  strips with the HPGe detector, as shown in Table 3. These correspond to an expected background of 0.2 events/year/kg from  $^{214}\text{Bi}$  and 1 event/year/kg from  $^{208}\text{Tl}$ , but it is expected that the measured contamination in these Se foils may again be localized and will be suppressed through data analysis. In the mean time a purification process is being developed at INEEL for potential future runs with several kilograms of Se.

Se enriched powder was used to make composite strips at ITEP, with the Type 3 backing film in sectors 06 and 07, and Type 1 in sector 08. The total mass of  $^{82}\text{Se}$  is  $(932 \pm 5)$  g.

- $^{130}\text{Te}$  source

The Te was enriched ( $89.4 \pm 0.5\%$  of isotope 130) by the production of  $^{130}\text{TeF}_6$  gas, followed by oxidation and reduction to obtain enriched  $\text{TeO}_2$  powder. The reason for  $^{130}\text{TeO}_2$  vs.  $^{130}\text{Te}$  is that it is easier to work. The Kurchatov Institute (Moscow, Russia) provided this powder to the NEMO collaboration after three separate purifications. For this sample the radioactivity limits for  $^{214}\text{Bi}$  and  $^{208}\text{Tl}$  were measured and a small contamination of  $^{228}\text{Ac}$  ( $^{232}\text{Th}$  decay chain) was

detected suggesting that the limit on  $^{208}\text{Tl}$  is close to a value which NEMO 3 should measure (see Table 3). Composite strips were made with the Type 1 backing film. A total mass of  $454 \pm 2$  g of  $^{130}\text{Te}$  was placed in sectors 09 and 17.

- $^{116}\text{Cd}$  source

Metallic enriched cadmium ( $93.2 \pm 0.2\%$  of isotope 116) was obtained again by the centrifuged separation method. Part of the sample had been measured with the NEMO 2 prototype [14]. Another part was purified by a distillation technique.

Despite the metallic quality of the cadmium source, strips were glued between Mylar foils to provide mechanical strength in the vertical position. A total mass of  $(405 \pm 1)$  g of  $^{116}\text{Cd}$  was placed in sector 18.

- $^{150}\text{Nd}$  source

The  $^{150}\text{Nd}_2\text{O}_3$  powder was provided by INR (Moscow, Russia), after enrichment ( $91.0 \pm 0.5\%$  of isotope 150) by electromagnetic separation and chemical purification. Radioactivity measurements (see Table 3) showed  $A(^{214}\text{Bi}) < 3.0$  mBq/kg (the maximum level of contamination required for NEMO 3 is 83 mBq/kg) but there was a small contamination of  $^{208}\text{Tl}$  ( $(10 \pm 2)$  mBq/kg instead of  $A(^{208}\text{Tl}) < 5.5$  mBq/kg for NEMO 3). As a consequence, this source will be used to check the ability of NEMO 3 to measure internal backgrounds.

The one neodymium composite strip (number 6 of sector 05) is made with 40.2 g of enriched  $\text{Nd}_2\text{O}_3$  powder and backing films of Type 1. This gives a total mass of  $37.0 \pm 0.1$  g of  $^{150}\text{Nd}$ .

- $^{96}\text{Zr}$  source

Enriched zirconium was obtained by an electromagnetic separation technique, with the samples averaging  $57.3 \pm 1.4\%$   $^{96}\text{Zr}$ . The samples were a powder of  $^{96}\text{Zr}_2\text{O}_2$ , from two different origins.

The first sample came from ITEP and was measured in the NEMO 2 prototype. Some contamination of  $^{40}\text{K}$ ,  $^{228}\text{Ac}$  and  $^{208}\text{Tl}$  was measured. Similar to the Se contaminants they

were concentrated in “hot-spots” and removed in data analysis [15]. The  $^{96}\text{ZrO}_2$  powder was recovered from NEMO 2 foils and purified using a chemical process. It represents 9.6 g of  $\text{ZrO}_2$  or  $4.1 \pm 0.1$  g of  $^{96}\text{Zr}$ . The second sample comes from INR (Moscow, Russia) and is 12.4 g of  $\text{ZrO}_2$  or  $5.3 \pm 0.1$  g of  $^{96}\text{Zr}$ .

The zirconium composite strips were made with enriched  $\text{ZrO}_2$  powder and backing films of Type 2. The strip is the seventh in sector 05. The total mass of  $^{96}\text{Zr}$  is  $9.4 \pm 0.2$  g.

- $^{48}\text{Ca}$  source

A  $\text{CaCO}_3$  sample is enriched in the isotope calcium 48 ( $73.2 \pm 1.6\%$ ). It was produced by electromagnetic separation methods in Russia. Additionally, a purification process was developed collaboratively by JINR and the Kurchatov Institute. It removes  $^{226}\text{Ra}$ ,  $^{228}\text{Ra}$ ,  $^{60}\text{Co}$  and  $^{152}\text{Eu}$ , as well as elements from the uranium and thorium decay chains. The measured purification factors for  $^{226(228)}\text{Ra}$ ,  $^{60}\text{Co}$  and  $^{152}\text{Eu}$  are greater than 1300, 3300 and 250, respectively. After the purification process, with 64 g of enriched  $\text{CaCO}_3$ , JINR had a yield of 42.1 g of enriched  $\text{CaF}_2$  powder.

The first portion (24.6 g of enriched  $\text{CaF}_2$ ) of this powder was used for radioactivity measurements with HPGe studies in the LSM. Only limits were obtained (see Table 3).

The second portion of this powder (17.5 g) was used to make nine 40 mm diameter disks. Mylar was again used and cut in the shape of the disks. To create the calcium portion of strip 25% of the seventh foil was populated with this material in sector 05. The disks were glued between two Type 2 backing films. In total there is  $6.99 \pm 0.05$  g of  $^{48}\text{Ca}$ .

- $^{\text{nat}}\text{Te}$  and copper sources

The foils of  $^{\text{nat}}\text{TeO}_2$  placed in the detector allows the NEMO collaboration to measure the external background for  $^{100}\text{Mo}$ . The effective  $Z$  of these foils ( $^{\text{nat}}\text{TeO}_2 = 43.2$ ) is nearly the same as that of the molybdenum foils ( $Z(\text{Mo}) = 42$ ). This is useful because the external  $\gamma$ -ray background can give rise to contamination processes, which are

all proportional to  $Z^2$ . Thus, the background for  $^{100}\text{Mo}$  and  $^{\text{nat}}\text{TeO}_2$  foils should give rise to similar event rates. In addition,  $^{\text{nat}}\text{TeO}_2$  has 33.8%  $^{130}\text{Te}$  and the  $\beta\beta 2\nu$  process expected has  $Q_{\beta\beta} = 2.53$  MeV. Thus these events would not enter the  $\beta\beta 0\nu$  region of interest for  $^{100}\text{Mo}$ . Consequently, a background subtraction is possible for the  $^{100}\text{Mo}$  foils using an analysis of the  $^{\text{nat}}\text{TeO}_2$  spectrum.

It is also useful to study  $\beta\beta$  processes for the  $^{130}\text{Te}$  part of  $^{\text{nat}}\text{TeO}_2$  (33.8%) compared to enriched  $\text{TeO}_2$ . Foils of  $^{\text{nat}}\text{TeO}_2$  were not purified, but radioactivity measurements showed limits lower than 0.17 and 0.09 mBq/kg for  $^{214}\text{Bi}$  and  $^{208}\text{Tl}$ , respectively, as shown in Table 3 (semiconductor purity levels).

The  $^{\text{nat}}\text{TeO}_2$  composite strips were made with Type 1 backing films for 5 strips in sector 08 and Type 3 for the 7 strips in sector 19. This gives a total mass of 614 g of  $^{\text{nat}}\text{TeO}_2$  or 166 g of  $^{130}\text{Te}$ .

The copper foil provides a similar study of external backgrounds for a smaller value of  $Z$ . The metallic copper source is very pure ( $A(^{214}\text{Bi}) < 0.12$  and  $A(^{208}\text{Tl}) < 0.04$  mBq/kg) with a mass of 621 g and was placed in sector 00.

## 2.2. Design of the calorimeter

### 2.2.1. Description

The three functions of the NEMO 3 calorimeter are to measure the particle energy, make time-of-flight measurements and give a fast trigger signal. The calorimeter is constructed with 1940 counters, each of which is made with a plastic scintillator, light guide and PMT (3" or 5"). The gains of the PMTs have been adjusted to cover energies up to 12 MeV. The plastic scintillators were chosen to minimize backscattering and for their radiopurity. The scintillators completely cover the two cylindrical walls which surround the tracking volume. There is also partial coverage of the top and bottom end-caps (also called petals).

The scintillator blocks are inside the helium-alcohol gas mixture of the tracking detector in order to minimize energy loss in the detection of electrons. The blocks are supported by a rigid frame, which allows the PMTs to be outside the helium environment. This configuration prevents rapid aging of the PMTs due to the helium.

The nomenclature for the calorimeter scintillator arrays is shown in Fig. 3. The arrays of scintillator for the calorimeter's petals are identified as L1 through L4 as one goes out radially. For the cylindrical walls of a sector, the internal wall array is designated IN and for the external wall there are the center (EC) and the edge (EE) arrays. There are seven types of scintillator which are distinguished by their different shapes which have been designed to fit the circular geometry of the NEMO 3 detector. All the scintillator blocks have a thickness of 10 cm which is a compromise to obtain a high enough efficiency (50% at 500 keV) for  $\gamma$ -ray tagging with plastic scintillators without loss of transparency of the scintillation light for the electron energy resolution (electrons from double beta decay being detected only in the entrance face of the scintillator block). The  $\gamma$ -ray tagging allows the measurement of the residual radioactivity of the source foil as well as rejecting background events.

### 2.2.2. Scintillator and light guide characteristics

The INR Kiev–Kharkov collaboration (Ukraine) was given the charge of producing the 480 end-cap scintillators and JINR was assigned the 1460 wall scintillators. The chemical nature of the material using for scintillator production is the solid solution of a scintillating agent p-Terphenyl (PTP) and a wavelength shifter 1,4-di-(5-phenyl-2-oxazolyl)benzene (POPOP) in polystyrene. After studies in both production laboratories, the mass fractions of polystyrene, PTP and POPOP were chosen. These are, respectively, 98.75%, 1.2% and 0.05% for the end-caps scintillators and 98.49%, 1.5% and 0.01% for the blocks of the walls.

As performance objectives, the energy resolution  $\sigma(E)/E$  for 1 MeV electrons had to be better than 6.2%. This resolution was checked during production using 482 and 976 keV conversion electrons produced by a  $^{207}\text{Bi}$  source. After etching the blocks under water to obtain diffusive reflection at the surfaces, there was an improvement in the resolution by about 1%. The average values of the energy resolution were, respectively, 5.1% for IN blocks and 5.5% for EE and EC blocks. To ensure the use of scintillators with the best resolution, a greater number of scintillator blocks

were produced than necessary: 1093 IN blocks for 680 used (62%), 994 EE blocks for 520 used (52%) and 428 EC blocks for 260 used (61%). In order to compare the performance of the different types of scintillator several tests were made such as optical transmission. For a 10 cm thick samples from Dubna, the light transmission was on average 75% and always greater than 70% for the wavelength 420 nm (see Fig. 6). The radiopurity of the scintillator was measured and found to be, respectively, 430 and 60 times lower in  $^{214}\text{Bi}$  and  $^{208}\text{Tl}$  activity than the PMTs used to read it out, which are also low radioactivity PMTs (see Table 4). The scintillator blocks were then sent to CENBG and IReS to mount the blocks with the best resolution on the walls and petals of the detector.

For the light guides optical polymethylmethacrylate (PMMA) was manufactured for the experiment and used for the scintillator and PMT interface. This also protects the PMTs from helium. The light transmission through the guides is 98% in the wavelength range 380–420 nm. To ensure rigidity the light guide is glued to an iron ring, which provides a pressfit between the guide and the petal or wall.

### 2.2.3. Photomultiplier tube characteristics

Development of low background PMTs was begun in 1992, in a collaboration between different

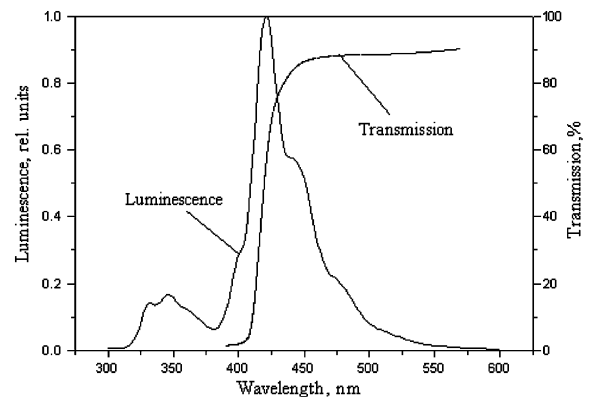


Fig. 6. Luminescence and transmission spectra of polystyrene-based plastic scintillators, such as that used in the wall blocks, but not a NEMO 3 block, rather a cylinder 10 cm long and 3 cm in diameter.

Table 4  
Total radioactivity, in Bq, for all NEMO 3 Hamamatsu photomultipliers

Total activity in Bq	$^{40}\text{K}$	$^{214}\text{Bi}$	$^{208}\text{Tl}$
3" PMTs R6091-1040 pieces (230 g/PMT)	354	86	5.2
5" PMTs R6594-900 pieces (385 g/PMT)	477	216	12.6
$\Sigma$ PMTs	831	302	17.8

manufacturers and physicists studying dark matter, double beta decay and neutrino oscillations. The selection criterion for the low radioactivity glass was for the contamination in  $^{40}\text{K}$ ,  $^{214}\text{Bi}$  and  $^{208}\text{Tl}$  to be lower than 1.7, 0.83 and 0.17 Bq/kg, respectively. The Hamamatsu company was chosen to produce the PMTs for NEMO 3, with the radiopurity of their glass being 100–1000 times better than standard glass (see Table 4). The other parts of their PMTs also have very low contamination (see Section 2.8 for the radioactivity measurements of the PMTs).

The IN, L1, L2 and L3 scintillator blocks were coupled to R6091 3" PMTs (230 g, 1040 pieces). These tubes have 12 dynodes and a flat photocathode. The EE, EC and L4 scintillator blocks were coupled to R6594 5" PMTs (385 g, 900 pieces). These 5" tubes have 10 dynodes and a hemispherical photocathode for structural integrity and thus need a second interface guide to match the design between the PMT and the light guide.

The Hamamatsu PMTs were chosen not only for their low background but also for their performance. A dedicated test station using a  $\text{H}_2$  lamp was developed. The energy and time resolutions were measured at 1 MeV, the average values were, respectively, 4% and 250 ps. The linearity of the response of the PMTs was studied as a function of the energies between 0 and 12 MeV. Also, the symmetry and the uniformity of the photocathode was investigated and finally the noise at the minimal threshold, 10 mV ( $\sim 33$  keV). As a consequence of 1 year of tests of the PMTs, 49 (2.5%) were rejected and replaced by Hamamatsu (five 5" and 44 3" PMTs).

#### 2.2.4. Preparation and installation of the scintillator blocks

A visual check on the color of the block was made. Then five layers of 70  $\mu\text{m}$  thick Teflon ribbon were wrapped around the four lateral faces of the scintillator block to diffusely scatter the scintillation light for improved light collection.

The energy resolution and the peak position at 1 MeV were checked for several locations on the entrance face of the block with an electron spectrometer using a  $^{90}\text{Sr}$  source. The spectrometer had an intrinsic energy resolution of 0.6%. This test identified and rejected blocks with inhomogeneities.

All six faces of the blocks, with the exception of the contact region for the light guide, were covered with sheets of aluminized Mylar. The Mylar not only protects the scintillators from ambient light and from light produced by Geiger propagation plasma in the tracking region, but also enhances the light reflection inside the scintillator, while minimizing energy lost by the electrons at the entrance face.

After gluing<sup>2</sup> the scintillator block to the petals and the walls, the peak position and energy resolution at 1 MeV were measured at the center of each block, using the electron spectrometer. This information was used to identify particular scintillator block and PMT combinations so as to obtain an energy resolution for the calorimeter which was as uniform as possible. The details of the performance of the calorimeter are given in Section 3.4.

#### 2.2.5. Assembly of the PMTs in the LSM

Once a sector was transported to the LSM, the 3" PMTs were glued directly to the light guides, while the 5" PMTs first had the interface guide glued to the light guide and then the interface/light guide combination glued to the 5" PMTs. After a check to see that the system was light-tight, a  $\mu$ -metal shield was placed around each PMT.

<sup>2</sup>A systematic check of the radiopurity for all the glues used in the NEMO 3 detector was carried out in the LSM [16].

### 2.3. The tracking detector

The tracking volume of the NEMO 3 detector is made of layers of vertical drift cells working in Geiger mode. After a long period of research and development at LAL, which had the responsibility for the tracking portion of the detector, the optimal parameters were identified for the best resolution and efficiency while minimizing multiple scattering effects. This optimization involved a balance between two parameters which contribute to aging effects of the wires. The first is the diameter of the cell's wires which needs to be as low as possible for better transparency in the tracking device. The second is the proportion of helium and alcohol in the gas mixture.

#### 2.3.1. Elementary Geiger cell

The cross-section of each cell is “octagonal” in design with a diameter of 3 cm that is outlined by 8 wires, as shown in Fig. 7. The basic cell consists of a central anode wire surrounded by the 8 ground wires, which belong to four adjacent cells to minimize the number of wires. However, between layers an extra ground wire was added to each cell to avoid electrostatic cross talk. All the wires are stainless steel, 50  $\mu\text{m}$  in diameter and 2.7 m long. The wires are strung between the two iron petals of each sector which form the top and bottom of the detector (see Fig. 3). On each end of the cell, there is a cylindrical cathode probe, which will be referred to as the cathode ring and can be seen in Figs. 4 and 7. The cathode ring is 3 cm in length and 2.3 cm in diameter. The anode wire runs through the center of this ring while the ground wires are supported just outside the ring. If one compares NEMO 3 to the previous prototypes NEMO 1 and NEMO 2, there is a new mechanism for securing the wires in the petals. The advantages of this new mechanism are that it allows easy wire installation, avoids the radioactivity of solder, and provides simple serviceability if replacement is necessary.

The cells work in the Geiger mode with initially a mixture of helium gas with ethyl alcohol. The characteristic operating voltage for the anode wires is 1800 V. When a charged particle crosses a cell the ionized gas yields around six electrons

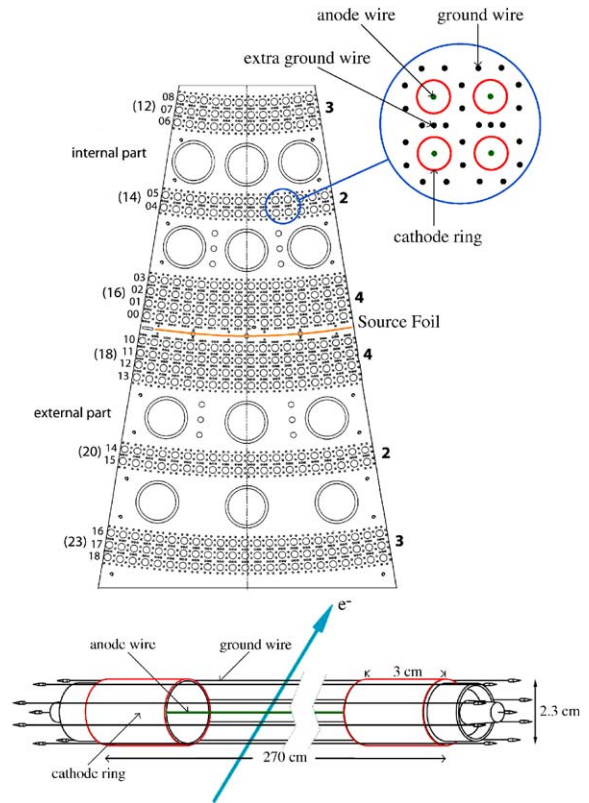


Fig. 7. Top view of one petal of the NEMO 3 sectors with a detail of four Geiger cells and view of an elementary Geiger cell. The basic cell consists of a central anode wire surrounded by eight ground wires, which belong to four adjacent cells, with an extra ground wire between layers as detailed in the right top of the figure. All the wires are 50  $\mu\text{m}$  in diameter and 2.7 m long. On each end of the cell is the cathode ring, 3 cm in length and 2.3 cm in diameter. The anode wire runs through the center of this ring while the ground wires are supported just outside the ring. One can see the “4-2-3” configuration, with nine layers on each side of the source foil numbered 00–08 and 10–18, respectively, for the internal and external parts starting from the source foil (in brackets are the number of cells in each layer).

per centimeter. These electrons drift towards the anode wire at a speed of about 2.3  $\text{cm}/\mu\text{s}$  when the electrons are close to the anode. When they are far away from the anode wire the mean drift velocity is around 1  $\text{cm}/\mu\text{s}$ , because the layout of the wires (field and ground) establishes a varying electric field within each cell.

Measurements of these drift times are used to reconstruct the transverse position of the particle



in the cells. The Geiger regime has a fast rise time for the anode pulse (around 10 ns) which can be used with a fixed threshold to provide a good time reference for the TDC measurements (see Section 2.4). In the Geiger regime, the avalanche near the anode wire develops into a Geiger plasma which propagates along the wire at a speed of 6–7 cm/ $\mu$ s, depending on the working point (Geiger plateau) which is a function of the gas mixture and operating voltage. The arrival of the plasma at the ends of the wire is detected with the cathode rings mentioned above. The propagation times are used to determine the longitudinal position of the particle as it passes through the cell.

### 2.3.2. NEMO 3 tracking device

Tracking simulations in a 25 G magnetic field were investigated. The study revealed the optimum configuration for the layers of cells in the sectors of NEMO 3. Taking into account multiple scattering in the track reconstruction the result was four layers near the source foil followed by a gap, then two layers and another gap followed by three layers near the scintillator wall (the “4-2-3” layer configuration, see Fig. 7). Thus, there are nine layers on each side of the source foil to reconstruct tracks. The gaps between the groups of cell layers is due to the position of the plastic scintillators on the petals. The four layers near the source foil are sufficient to provide a precise vertex position. Two layers in the middle and three layers close to the plastic scintillator walls provide good trajectory curvature measurements.

### 2.3.3. Assembly and wiring of a sector

To suspend the wire cells the iron petals have an intricate pattern of holes drilled into them in order to support the 4-2-3 layer configuration. The sectors were wired in a class 10,000 clean room. Studies with prototypes confirmed the need for very high quality wire for proper plasma propagation. To fulfill this requirement a special production run of a 200 km long stainless steel wire, that was 50  $\mu$ m in diameter, was contracted.<sup>3</sup> Precision in the diameter is better

than 1%. Wires were strung layer by layer, alternating ground and anode wires. The wiring of one sector took about four weeks for the 1991 wires.

Cells are of high quality if two conditions are satisfied simultaneously: at operating voltage the counting rate is free of secondary triggers and electrical discharges while having the Geiger plasma propagated to both extremities of the cell. A special container measuring 6.4 m<sup>3</sup> was used to test each of the 20 sectors. The measured counting rates in the cells using cosmic rays is around 60 Hz compared to 0.2 Hz in the LSM before the coil and shields were added. Thus a test for one week at LAL corresponds to several years of operation in the LSM. As a result of the anode tests, it was found that on average 10 of the 340 anode wires were replaced per sector. Fewer than 10 ground wires per sector needed to be replaced. This exercise also demonstrated the efficiency of cell repair.

The final step, to ensure a tight seal to contain the helium, used silicon RTV to outline the regions to be sealed, and then Araldite. A gas seal was also formed between the petals and walls, at the exterior of the sectors.

## 2.4. Electronics, trigger and data acquisition systems

The NEMO 3 detector has calorimeter and tracking detector independent electronics and data acquisition systems with a trigger system that can be inter-dependent. The electronics, trigger and data acquisition are separated into modules which share a VME bus. This design permits not only  $\beta\beta$  runs, but also different tests to adjust and calibrate the detector.

### 2.4.1. Calorimeter electronics

The PMT bases are designed with a progressive voltage divider to improve the linearity under conditions of high current. Tests carried out at the IReS laboratory identified fixed sets of resistors for the PMT bases which control the voltage between the photocathode and the first dynode so as to optimize the time resolution.

<sup>3</sup>Trakus factory, Germany.

Three large power supplies from C.A.E.N.<sup>4</sup> are used to supply the HV for the 1940 PMTs. Each HV channel is shared by three PMTs via a distribution board. The three PMTs must be similar in gain and fine tuning is done with two carefully selected fixed resistors on the distribution board for each PMT. Data taken with a <sup>207</sup>Bi source was used to set the PMTs gains. There are nine distribution boards per sector and each board has four HV channels that in turn supply 12 PMTs.

The 97 PMTs of each sector are divided by the source foil into the interior and exterior regions. A total of 46 PMTs are used for the interior region of which 12 PMTs are on the top and bottom petals. The exterior region is covered with 51 PMTs, again with 12 PMTs on the top and bottom petals. Thus, there is a total of 40 half-sectors for which front-end electronics boards are designed. The corresponding 40 mother boards are housed in three VMEbus crates and each mother board supports 46 or 51 analog-NEMO (ANEMO) daughter boards.

The ANEMO boards have both a low and a high threshold leading edge discriminator (the slewing issue will be addressed at Section 2.5.7). If the PMT signal exceeds the lower level threshold it starts a TDC measurement and opens a charge integration gate for 80 ns. The high threshold discriminator is adjustable up to 1 V but generally runs at 48 mV corresponding to 150 keV. The high threshold discriminator works as a one shot that delivers an event signal to the mother board.

Each mother board in turn provides an analog signal to the trigger logic which reflects the number of channels that have exceeded the upper threshold. The signal strength is 1 mA per channel. This level is used to trigger the system (first level trigger) if the desired multiplicity of active PMTs is achieved. The trigger logic then produces a signal called STOP-PMT, which is sent to all the calorimeter electronic channels, to save their data. So the TDCs are stopped and the integrated charge is stored. Then digital conversions begin. At the same time, a signal is sent to the calorimeter

acquisition processor, which permits the read out of the digitized times and charges for the active channels.

The analog-to-digital conversions of the charge and the timing signal are made with two 12-bit ADCs. The energy resolution is 0.36 pC/channel ( $\sim 3$  keV/channel) and the time resolution is 53 ps/channel. If any PMT signal exceeds the high level threshold then the TDC measurement and charge integration are aborted and the system resets after 200 ns.

#### 2.4.2. Tracking detector electronics

The Geiger electronics are divided into two types of boards. The first is for secondary voltage distribution, which provides 1800 V to the anode wires. Included on the secondary distribution boards are the analog signals from the anode wire and the two cathode rings. These boards receive high voltage from two of the C.A.E.N. power supplies.<sup>5</sup> The second type of board is for the tracking electronics and is an acquisition board which is connected to the distribution board. It uses ASICs<sup>6</sup> and has an interface with a 50 MHz clock (TDCs provide a 20 ns LSB).

The functions of the acquisition board are first amplification and then discrimination of analog signals coming from the distribution board. Time measurements for each cell are acquired for the anode wire and the two cathode rings. Note that the two cathode times are identified as  $t_{LC}$  and  $t_{HC}$  where LC and HC stand for low and high cathode times. The low one corresponds to the cathode ring on the bottom of the detector and the high for the top.

Each of the 20 sectors needs the following electronics. Eight secondary distribution boards receive a total of 15 daughter boards, of which five for the anode, five for LC and five for HC signals. The five sets of three different daughter boards services eight cells per set, so that there are 40 cells per distribution board. Then each sector also needs eight acquisition boards, which receive 10 analog ASIC and 10 digital ASIC circuits, with

<sup>4</sup>C.A.E.N. HV power supply type SY527 10 boards A938 AP, 24 channels each, with AMP multicontact connectors.

<sup>5</sup>C.A.E.N. HV power supply type SY527 with A734P boards, 16 channels each.

<sup>6</sup>Application Specific Integrated Circuit.

each ASIC handling four cells, so 40 cells per board.

Each of the four channels of the analog ASIC<sup>7</sup> is used to amplify the anode and two cathode signals by a factor of 60, and to compare them to anode and cathode thresholds generated by a software programmable 8-bit DAC. For signals exceeding the thresholds, a comparator provides a TTL signal which is sent to the TDC scalers of the digital ASIC. There are four TDCs for each of the four channels of the digital ASIC.<sup>8</sup> The first three are for the anode ( $tdc_A$ ), low cathode ( $tdc_{LC}$ ) and high cathode ( $tdc_{HC}$ ) contents which are measured with a 12-bit TDC and give times between 0 and 82  $\mu$ s. The alpha TDC ( $tdc_\alpha$ ) is 17-bits, which can provide time measurements between 0 and 2.6 ms. It is used for  $\alpha$ -particle tagging (see Section 1.3.1).

The anode signal starts the TDCs and creates an OR signal (called HIT) for all the cells of a layer of a given sector; so 360 TTL signals are sent to the T2 trigger (see Section 2.4.3).

The propagation of the Geiger plasma is detected by the cathode rings. These signals stop their respective cathode TDCs and give  $tdc_{LC}$  and  $tdc_{HC}$  values. Physical propagation times are proportional to these values:

$$t_{LC} = [tdc_{LC} \times 20] \text{ ns.} \quad (6)$$

$$t_{HC} = [(tdc_{HC} \times 20) - 17.5] \text{ ns.} \quad (7)$$

The time constant, 17.5 ns, is removed from  $t_{HC}$  to take into account the difference in cable lengths: the low cathode cables are 6 m and high cathode cables 9.5 m.

Concerning the anode signal, there are two cases which have to be distinguished. The anode signal can exceed its threshold before or after the arrival of the STOP-A signal which comes from the trigger (see Section 2.4.3). In the first case, for  $\beta$ -type events, the STOP-A signal is used to stop the  $tdc_A$  channels which have received an earlier start signal. Anode times  $t_A$ , correspond to the transverse drift time given by:

$$t_A = [(tdc_{\max} - tdc_A) \times 20] \text{ ns} \quad (8)$$

where  $tdc_{\max}$  corresponds to 6.14  $\mu$ s.

In the second case, for  $\alpha$ -type events, all Geiger cells not already triggered can register delayed hits which occur after the STOP-A has been received for up to 704  $\mu$ s. Anode signals exceeding their threshold start not only their anode and cathode TDCs but also their alpha TDCs ( $tdc_\alpha$ ).

Cathode signals stop the cathode TDCs and give  $tdc_{LC}$  and  $tdc_{HC}$  values, but the anode and alpha TDCs are stopped by the STOP- $\alpha$  signal coming from the trigger. As a consequence, in this case the  $tdc_A$  and  $tdc_\alpha$  have the same value modulo 4096 for these cells. The corresponding alpha time  $t_\alpha$  is then given by:

$$t_\alpha = [(tdc_{\alpha_{\max}} - tdc_\alpha) \times 20] \text{ ns} \quad (9)$$

where  $tdc_{\alpha_{\max}}$  corresponds to  $\sim 704 \mu$ s.

#### 2.4.3. The NEMO 3 trigger system

The trigger system was developed by LPC. It receives one analog signal from each of the 40 half-sectors that is proportional to the number of PMTs that have exceeded their high threshold in that sector. The 40 signals are summed resulting in an analog signal. The trigger then goes onto the second level which involves the Geiger layers. In this case 360 channels are read out by treating each Geiger layer in each sector as a bit, which is on if the layer is hit. This information allows the use of a rough track recognition program to be run on the available Geiger cell information. It is then possible to refine the identified tracks by spatially connecting the Geiger cells and triggered PMTs.

Timing constraints and trigger strategy lead to a two level trigger system for normal running with a third level for calibration runs.

The *first level* (T1) of the trigger, is embedded on the T1-3 board, and is based on the number of PMTs required to initiate a readout. It is used to identify the number of active scintillators by using the summed current from the 40 analog signals to define the multiplicity of the event (MULT).

If the trigger logic encounters a multiplicity higher than that set by the MULT threshold up to 20 ns after the first triggered PMT, T1 generates the STOP-PMT signal, which is the timing reference of the experiment, with an electronic accuracy better than 150 ps.

<sup>7</sup>1.20 micron technology from AMS inside PLCC 44 boxes.

<sup>8</sup>1.00 micron technology from ES2 inside PLCC 68 boxes.

The *second level* ( $T2$ ) consists of track recognition in the Geiger layers (GG), using the 40 half-sectors. The track recognition is first performed on a per half-sector basis. Nevertheless, the probability for an electron to cross more than one sector is high, so tracks that cross two adjacent half-sectors are searched for in a second step. Thus, there are two secondary levels.

The first level search is between four different possible tracking patterns, which correspond, respectively, to a long track, a short track near the foil, a short track near the scintillator block or no track; the second level consists of making special associations between adjacent half-sectors. For example a long track in a half-sector and any kind of track or no track in the adjacent half-sector. One possibility is to use two short tracks in two adjacent half-sectors, one near the foil and the other near the calorimeter walls, which allows the trigger to select a full track contained in more than one sector.

This level is embedded on the T2I (internal) and T2E (external) boards, which receive 180 HIT signals each and provide nine logical signals from a logical OR which lasts for  $3\mu\text{s}$  on the cells of each layer. If the trigger logic is satisfied for the chosen track condition, a second level local trigger is generated. The T2 level conditions on the T2I/E boards are set in programmable memories.

The *third level* ( $T3$ ), which is only used for calibration runs, is embedded on the T1-3 board and checks on the possible coincidence between pre-tracks from T2's second stage and fired PMT half-sectors. This level selects electron tracks coming from radioactive sources installed in the calibration tubes. It is implemented in hardware without the possibility of changing the algorithm.

For the case of an active PMT and Geiger cell trigger condition (PMT+GG), if the second level trigger is detected, the STOP-A signal is sent to Geiger acquisition boards with the programmable delay. This delay is set to  $6.14\mu\text{s}$  after the STOP-PMT signal. Then two trigger signals are sent to the Geiger and calorimeter electronics with a programmable delay set to  $6.14\mu\text{s}$  after the STOP-PMT signal. The first signal stops the automatic time-out which occurs  $102\mu\text{s}$  after the STOP-A signal. The second permits the

digitization of the analog signals of the activated PMTs. In case these signals are not received there is an automatic reset of each of the PMT channels which have started measurements. Finally, the STOP- $\alpha$  is sent to the Geiger acquisition boards with a fixed delay of  $710\mu\text{s}$  after the STOP-PMT signal (see Fig. 8).

#### 2.4.4. The NEMO 3 data acquisition system

The control and readout of the calorimeter and Geiger cell crates is performed with the inter-crate VICbus and two CES RIO 8062 computer modules equipped with PowerPC 604E-300 MHz CPU chips. The data acquisition system is based on *Cascade* [17] operating under the Lynx-OS software package developed at CERN. It uses two boards: Corbo PMT for the calorimeter readout trigger and Corbo GG for the track detector readout trigger. The two independent acquisition processors collect information in parallel. After the processors have read out the event and deactivated their “busy” signal, the trigger system reinitializes its logic electronics for the next event. Data buffers for the calorimeter and Geiger cells are then sent to the event builder processor (EVB) via the PVIC bus (multidrop PCI-to-PCI high speed link), as described in Section 3.2.

#### 2.4.5. Survey of the experiment

Monitoring and control of the experiment from remote sites is possible with two dedicated PCs in the LSM. The two PCs also operate locally. The tasks of these two PCs are not overlapping. The first controls the gas system of the tracking chamber, the current in the magnetic coil and the high voltage on the Geiger and PMT boards. The second controls the on/off power for the acquisition boards and crates, the high voltage crates and the uninterruptible power supply.

#### 2.4.6. The NEMO 3 database: NEMO DB

The MySQL database management system is used for NEMO 3. Data synchronization in the NEMO DB server network is based on the replication concept of the MySQL package. Here any number of servers can be replicated and can transfer data from one primary server. The structure of the NEMO MySQL servers includes

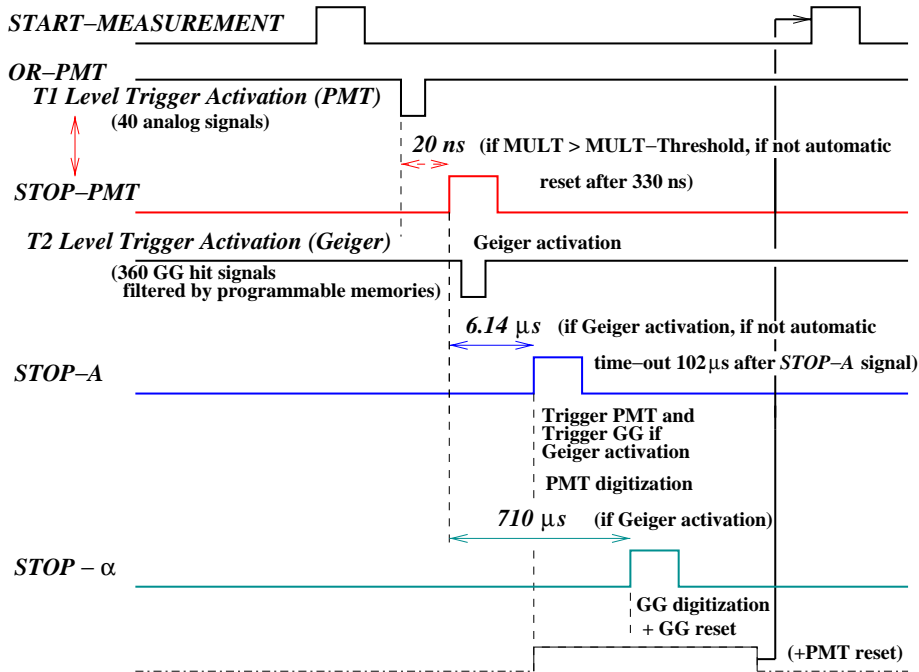


Fig. 8. Chronogram of the NEMO 3 trigger system (for the PMT + GG trigger condition).

the primary server at the LSM for information stored in the on-line database, the main server at Lyon CCIN2P3<sup>9</sup> which contains all the data, and a set of local servers mirroring the main server.

The NEMO DB contains the electronic logbook of the runs, the calibration parameters of scintillator counters and Geiger cells, as well as other information about the run conditions.

## 2.5. Energy and time calibration of the counters

### 2.5.1. Introduction

In order to measure accurately the absolute energy released in a double beta decay ( $Q_{\beta\beta}$ ), a calibration procedure was established. The solution for NEMO 3 is to use radioactive sources that can be introduced into the detector and present only during runs dedicated to calibration. These absolute energy measurements run for extended periods and take place only two or three times a

year. Thus, daily studies of the stability of the counters are done with a laser survey system.

Timing information is used to discriminate between external and internal events for background studies (see Section 1.3). The relative timing offsets for each of the 1940 counters has to be determined, using particles emitted in coincidence from  $^{60}\text{Co}$  radioactive sources. Particle times-of-flight are also corrected for several effects specifically the amplitude corrections due to leading edge discriminators (called time-energy corrections) and TDC slope corrections. These corrections are also checked with the laser survey system.

### 2.5.2. Mechanics of the calibration tubes

Each of the 20 sectors of the detector is equipped with a vertical tube made of flattened copper that is located along the edge of the source foils (see Fig. 3) and three pairs of kapton windows: one window of the pair is oriented towards the internal wall and the other towards the external one. The size of the windows ( $\sim 500 \text{ mm}^2$ ) and their vertical positions ( $z =$

<sup>9</sup>Centre de calcul de l'IN2P3: computer center of the institute for nuclear and particle physics.

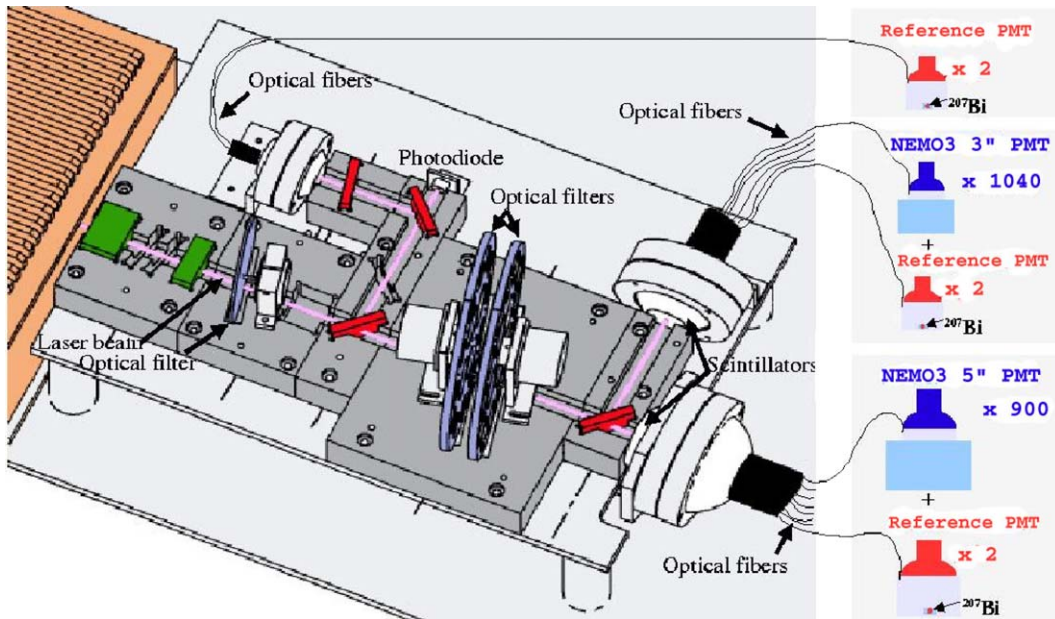


Fig. 9. The laser calibration system.

–90,0 and +90 cm with an accuracy better than 1 mm) have been chosen to obtain an approximately uniform illumination of the scintillator blocks by three radioactive sources placed inside the tube. The source carrier is a long narrow delrin rod supporting three source holders which are introduced into the copper tube from the top of the detector, after the removal of some shields on the top.

### 2.5.3. Radioactive sources

For energy calibration of the counters, one needs radioactive sources which emit electrons. The choice was made to use  $^{207}\text{Bi}$  and  $^{90}\text{Sr}$  sources. Decay of the first one provides conversion electrons of 482 and 976 keV energy (K lines) suited for an energy calibration up to 1.5 MeV. The products in  $^{207}\text{Bi}$  decay are essentially  $\gamma$ -rays, thus the tracking chamber must be in operation to select electrons originating directly from the sources. To measure energies up to 3 MeV or more, one needs at least one additional calibration point, which is obtained using electrons from  $^{90}\text{Y}$  (daughter of  $^{90}\text{Sr}$ ) and measuring the end-point of the  $\beta$  spectrum at 2.283 MeV. This calibration does

not require pattern recognition because the events of interest are located in the tail of the spectrum, which can only contain electrons coming directly from the sources. Relatively intense sources are used here for short runs.

For timing calibration, the relative offsets for each channel are determined with a  $^{60}\text{Co}$  source, which emits two coincident  $\gamma$ -rays with energies of 1332 and 1173 keV. Spectra of arrival time differences are collected to establish time delays between the 1940 channels. This time calibration does not require the use of the tracking chamber and allows the use of relatively intense sources.

### 2.5.4. Laser calibration system

In an experiment such as NEMO 3, which requires stability for many years over a large number of PMTs, frequent tests of the detector's stability are of paramount importance. The objectives of the chosen laser calibration system,<sup>10</sup> as shown in Fig. 9, are first a daily check of the absolute energy and time calibration, which permits the calculation of the corrections

<sup>10</sup>MNL 202 laser from Lasertechnik Berlin; 200 kW, 10 Hz.

according to the emission peak. Next measurements of the PMTs linearity between 0 and 12 MeV are made and finally is determined the time-energy relation. To accomplish this, the shape of the laser signal has to be very similar to the one produced by an electron. Thus the laser light must be known with very high accuracy ( $<1\%$ ) and must be stable during the measurement. One needs also a precise calibration of the optical filter transmission for the energy range 0–12 MeV and a good common time reference (STOP).

The  $N_2$  laser wavelength of  $337 \pm 15$  nm was selected. Then the light beam is split into two parts. The first is sent to a photodiode, which monitors the laser light intensity. A variable optical attenuator is used to adjust the flux. The second beam goes through two optical filter wheels to simulate the full range of energy. This beam is then wavelength shifted to 420 nm and sent to the NEMO 3 PMTs by means of optical fibers. The shifter is a sphere of scintillator, wrapped in Teflon and aluminum to increase diffusive reflections, used to mimic the signal of electrons in the scintillators. Each optical fiber<sup>11</sup> is divided into two strands and the optical distance between these two is adjustable using individual attenuators, which allow the distribution of the same flux of light to all the counters. Six reference counters (independent of the NEMO 3 calorimeter) equipped with  $^{207}\text{Bi}$  sources allow the monitoring of the laser by measuring energies of both the laser and the 976 keV conversion electrons emitted from  $^{207}\text{Bi}$ .

The daily laser procedure is carried out in two steps. The first one is during the run under standard conditions for the acquisition of  $\beta\beta$  events ( $\beta\beta$  run). It consists in stabilizing the laser and checking parameters, such as photodiode pedestal and laser light. During this step the flux can be corrected if necessary. The second step is made at the end of the  $\beta\beta$  run. It consists of a pedestal measurement for the PMTs,<sup>12</sup> then a rotation of two filter wheels to obtain a 1 MeV equivalent flux, this is followed by the acquisition

of the laser and  $^{207}\text{Bi}$  events. Finally the laser is turned off and the filter wheels moved to opaque settings. For “complete” calibration run up to 12 MeV, the procedure is only repeated few times during the year with different fluxes and changing the rotation of the two optical attenuator disks for each run.

#### 2.5.5. Absolute energy calibration method

Over the full 12 MeV range of energies measured by NEMO 3, the relation between the charge signal and energy deposited in the counter is not necessarily linear. The relation is, however, linear up to 4 MeV, where the greatest accuracy is required:

$$E = a(C - P) + b \quad (10)$$

here  $C$  is the ADC value of the scintillator and  $P$  is the pedestal. The energy calibration constants  $a$  and  $b$  are determined using at least two points from measurements with radioactive sources, while the relation for the energies greater than 4 MeV is determined using a “complete” laser calibration run.

The energy resolution is assumed to have essentially two contributions. The principal component originates from the statistical fluctuations of the scintillation photons and from the number of photo-electrons at the PMT anode. It increases as the square root of the energy. The second component is due to the instrumental effects which are energy independent. These two terms contribute to the resolution in quadrature in the form:

$$\sigma(E) = A\sqrt{E} \oplus B. \quad (11)$$

Using 60  $^{207}\text{Bi}$  sources ( $\sim 220$  Bq each) with the high threshold set at 48 mV ( $\sim 150$  keV), a 24 h run yields about 5000 events for each PMT with identifiable tracks. Then the positions of the two peaks, corresponding to the 482 and 976 keV conversion electrons, are extracted and the resolution is obtained as a result of a fit to the 976 keV line.

Using four  $^{90}\text{Sr}$  sources simultaneously ( $\sim 6$  kBq each) eight runs are taken with the sources in different positions and a threshold of 48 mV ( $\sim 150$  keV). For each PMT about  $5 \times 10^4$  events are used to form a spectrum (see top of Fig. 24). A

<sup>11</sup>Toray PFU-CD501-10-E.

<sup>12</sup>1940 PMTs from the NEMO 3 calorimeter and six PMTs for the reference counters.

fit to the high-energy tail of the spectrum is made with a function describing the shape of a single  $\beta$  spectrum of  $^{90}\text{Y}$ , convolved with the energy resolution function  $\sigma(E)$  and taking into account the mean energy loss of the electrons in the gas of the wire chamber.

Finally, these three results (two peaks and one end-point) from the calibration runs with  $^{207}\text{Bi}$  and  $^{90}\text{Sr}$  are combined to extract the parameters  $a$  and  $b$  of a linear calibration valid for the energy region up to 4 MeV. The results of energy calibration runs are presented in Section 3.4.

### 2.5.6. Energy corrections using the laser system

The laser procedure is carried out as a reference just after the calibration runs and gives a fiducial reference energy,  $E_0$ , for each counter (one assumes there is no correction to be applied to the  $b$  offset). At a later time  $t$  a new value of the energy,  $E_t$ , is measured:

$$E_0 = a_0(C_0 - P_0) + b \quad \text{and} \\ E_t = a_t(C_t - P_t) + b = e_{\text{corr}} \times a_0(C_t - P_t) + b$$

where  $e_{\text{corr}}$  is the correction factor to be applied. It represents the variation of the calibration slope of the counter as a function of time between  $t_0$  and  $t$ . This variation of the laser is determined by comparing the laser peak position ( $C_{\text{laser}}$ ) and the 976 keV peak position from the  $^{207}\text{Bi}$  ( $C_{\text{Bi}}$ ) between  $t_0$  and  $t$  for the six reference counters. Results are then transferred to the database.

The “real” energy value  $e_{(t)}^{(i)}$  for counter number  $i$  at instant  $t$  is finally given by:

$$E_{(t)}^{(i)} = [(C_{(t)}^{(i)} - P_{(t)}^{(i)}) \times a^{(i)} \times e_{\text{corr}(t)}^{(i)}] + b^{(i)}. \quad (12)$$

### 2.5.7. Time calibration

The timing response of two counters detecting two particles emitted in coincidence depends not only on the time-of-flight of each particle, but also on several effects which have to be corrected for.

#### • Time alignment of the counters

All PMTs must be aligned in time. The time taken for each PMT to respond to a signal

depends on the individual characteristics of the counter. In order to use only one time scale, an alignment procedure has been developed to obtain the individual time shifts  $\varepsilon^{(i)}$  ( $i = 1-1940$ ). The procedure to find  $\varepsilon^{(i)}$  uses  $\gamma$ -rays emitted in coincidence by a decay in a  $^{60}\text{Co}$  radioactive source and detected by a pair of scintillators. There is a common START in the electronics for both counters and the electronics uses a common STOP-PMT for all the counters, which allows the individual delays to be extracted.

In order to calculate the time-of-flight correctly, only one  $^{60}\text{Co}$  source of 15.5 kBq is used per run. Ten runs with different source positions are performed in order to cover all possible combinations of PMTs. A threshold of 150 mV ( $\sim 500$  keV) is set for the arrival time difference spectra and the relative timing offset  $\varepsilon^{(i)}$  for each counter  $i$  (see Section 3.4).

#### • Other corrections

The effect of leading edge discriminators is to induce a time-vs.-energy dependence, which can be described with a formula using four parameters

$$t(C) = p_1 - \frac{p_2}{p_3\sqrt{C} + p_4} \quad (13)$$

and taking into account the pulse shape. Determination of the parameters  $p_k^{(i)}$  ( $k = 1-4$  for counter  $i$ ) is accomplished through a “complete” laser run producing equivalent energies between 0 and 12 MeV. The relative timing offset  $\varepsilon^{(i)}$  for counter  $i$  is then included in the asymptotic value  $p_1^{(i)}$ .

The laser survey system is also used to obtain daily time response corrections for each counter, which correspond to TDC slope variations:  $t_{\text{corr}} = tdc_t - tdc_0$ .

Finally, the “real” time,  $T_t^{(i)}$ , used for a time-of-flight calculation for counter number  $i$  at instant  $t$  is:

$$T_{(t)}^{(i)} = tdc_{(t)}^{(i)} - t_{\text{corr}(t)}^{(i)} - t(C_{(t)}^{(i)}). \quad (14)$$



## 2.6. Coil and shields

### 2.6.1. Introduction

To reach the desired sensitivity for the effective neutrino mass, there must be no events ( $<0.1$ ) from external backgrounds in the energy range [2.8–3.2] MeV during 5 years of data collection. The external background contribution coming from neutrons is due to ( $\alpha, n$ ) reactions, spontaneous fission of uranium and the interaction of cosmic ray muons in the rocks. The other external background contribution is the  $\gamma$ -ray flux produced in the LSM, which has been studied using a NaI detector surrounded by different shields [18]. The origins of these  $\gamma$ -rays are natural radioactivity, radiative neutron captures and the bremsstrahlung of muons.

As shown in Section 2.8, the detector has been designed with stringent radiopurity for its construction materials. For the external background coming from  $\gamma$ -rays and neutrons, several studies were made with the NEMO 2 detector as well as the NEMO 3 simulations [19]. These have shown that there is a large reduction in these backgrounds given the following conditions to the experiment. A solenoid capable of producing a field of 25 G is surrounded by two external shields, the first one to reduce  $\gamma$ -ray and thermal neutron fluxes, the second to suppress the contribution of slow and fast neutrons. The design of the coil and shields allows for partial dismantling of the detector to access each sector.

### 2.6.2. The magnetic coil

The simulation of the fast neutrons coming from the laboratory into NEMO 3 was carried out with 20 cm of iron shield. The contribution to the  $\beta\beta 0\nu$  background by the  $\gamma$ -rays created from neutron captures leads mainly to ( $e^+e^-$ ) events and also to a few ( $e^-e^-$ ) events produced in the source foils. The detection by the calorimeter of the  $\gamma$ -rays associated with these events provides a high rejection efficiency (80%). A 25 G magnetic field, which provides the charge recognition rejects 95% of the ( $e^+e^-$ ) pair events.

The coil surrounds the entire detector and access to the detector was a necessary design consideration. Thus, the coil is made of 10 sections with 203

copper rings connecting every other sector to form one loop of the helix (see Fig. 1). The finished coil is cylindrical, 5320 mm in diameter, 2713 mm in height and has a mass of 5 tons ( $\sim 3.1$  tons of high radiopurity copper).

### 2.6.3. Iron shield

The iron shield is also made in ten sections (165 tons) with two end-caps (6 tons each). The lower end-cap is fixed and the upper one is removable. The iron shield is 20 cm thick, except for a few places where it is 18 cm on account of mechanical supports. The iron was selected for its radiopurity, as recorded in Table 6.

### 2.6.4. Neutron shield

The remaining ( $e^+e^-$ ) pair events (5% not rejected by curvature measurements) and the ( $e^-e^-$ ) events due to the  $\gamma$ -rays created by neutron capture can be suppressed only if the flux of neutrons inside the detector is decreased. NEMO 3's neutron shield is optimized to stop fast neutrons with an energy of a few MeV, it also suppresses thermal and epithermal neutrons.

The neutron shield is made of three parts, as shown in Fig. 1. The first one is situated below the central tower of the detector (not shown in the figure) and consists of paraffin 20 cm thick. The second part covers the end-caps below and above the detector, and consists of 28 cm of wood. The cylindrical external walls are covered with 10 large tanks containing borated water which are 35 cm thick and separated by wood 28 cm thick.

## 2.7. Mounting and assembly of the detector in the LSM

### 2.7.1. Supporting structure

The steel framework, which supports the NEMO 3 sectors, is made of two parts. It was installed in the LSM at the end of 1998 and supports the 20 sectors of the detector, the magnetic coil and the various shields. All the components of the framework were selected for their radiopurity. To properly enclose the active detector and have access to readout electronics in the narrow experimental hall, the detector was raised off the ground two meters. Thus the control

and readout electronics can be housed under the detector. This structure preserves proximity and serviceability of the electronics and detector.

### 2.7.2. Placing of the sectors on the supporting structure

Once the sectors were made helium tight, the anode and cathode cables were connected at LAL before being transported to the LSM, where PMTs were attached. After gluing and testing the PMTs, the sectors were carried inside the source mounting room and cleaned using alcohol and nitrogen gas.

The source frame, which supports the seven foils of each sector, was prepared simultaneously in the LSM clean room. This source frame was then mounted in the sector. Finally, the calibration tube was set in position and the sector was cleaned once again with nitrogen and closed with sheets of Mylar.

The source mounting room was then opened to move the sectors to the supporting structure. The calorimeter cables (HV and signal) were soldered to the PMT bases and to the distribution daughter boards. These operations were followed by the introduction of the plastic optical fibers into brass tubes which are present in each light guide of the calorimeter. Finally there was a thorough test of the connections for the calorimeter, the tracking detector and the laser system (both electrical and optical). During these procedures the sectors were filled with nitrogen to avoid deposition of impurities on the wires.

These tasks were previously checked in the year 2000 for three sectors (00, 18 and 19). The 17 remaining sectors of NEMO 3 were gradually installed and tested until August 2001. The 20 sectors were then placed in their final positions and the helium seals made using RTV glue.

The total fiducial volume inside the tracking detector is 28 m<sup>3</sup> (excluding the scintillator volume). The detector was filled with gas in December 2001, using a fast flushing of helium gas (5 volumes), followed by introduction of ethyl alcohol in the gas regulation system. The whole process took approximately 24 h. A constant pressure of gas was maintained with a flux of the order of 130 l/h until December 2002. The magnetic coil was installed in February 2002 and

$\gamma$ -shield in April 2002. Finally, the installation of the neutron shield was completed in February 2003. Between each step,  $\beta\beta$  and calibration runs were taken to monitor stability and the effectiveness of the shields for comparisons with simulations.

Data collection was temporarily stopped in December 2002 to make several improvements. These involved changes in HV power supplies for the calorimeter PMTs' overvoltage protection, while noise and gain adjustments were made on several PMTs. Helium leaks were sealed and there was an addition of argon into the gas mixture of the tracking detector in order to improve the Geiger cell stability and efficiency of the plasma's longitudinal propagation as well as limiting the aging problems. At the same time, the proportion of quencher in the mixture was reduced from 40 to 39 mbars partial pressure (ethyl alcohol at 14 °C instead of 15 °C). The gas mixture used in the day-to-day running is now He with Ar (with  $V(\text{Ar})/V(\text{He}) = 1\%$ ) and ethyl alcohol as the quencher at a flux of 300 l/h. An overpressure of  $\sim 10$  mbars is maintained to flush contaminants from the surrounding gas volume.

In mid-February 2003, new  $\beta\beta$  runs commenced under improved conditions, with the coil and both shields.

### 2.8. Radiopurity of the detector

$\gamma$ -ray spectra were acquired using low background HPGe detectors located at CENBG and in the LSM. These HPGe spectrometers [12] typically use the "Marinelli" geometry to measure the abundance of selected isotopes in the decay chains via the strength of selected gamma lines. The "Marinelli" geometry requires a large quantity ( $\sim 1$  kg) of the material in question to be arranged around the Ge crystal to obtain a large angle acceptance.

#### • Radioactivity measurements of the source foils

A 400 cm<sup>3</sup> HPGe spectrometer in the LSM has a sensitivity capable of reaching 0.2 mBq/kg of <sup>214</sup>Bi and 0.06 mBq/kg of <sup>208</sup>Tl in a month with a 1 kg sample. The maximum allowed levels of <sup>214</sup>Bi and

$^{208}\text{Tl}$  contamination in the Mo sources are given in Eqs. (2) and (3). The level of sensitivity necessary for  $^{214}\text{Bi}$  was achieved, but not for  $^{208}\text{Tl}$ . A solution could be reached by counting for more than one month but the collaboration has decided to make a compromise between the source measurement and the detector's construction. Radioactivity measurements for all the NEMO 3 sources are summarized in Table 3. Only the lower limits obtained for  $^{100}\text{Mo}$  are presented, for both the metallic and composite strips. In this table it can be seen that for  $^{208}\text{Tl}$  only limits have been obtained except in  $^{82}\text{Se}$  and  $^{150}\text{Nd}_2\text{O}_3$  strips. In the case of  $^{82}\text{Se}$ , the presence of "hot-spots", which can be suppressed by analysis, is anticipated. For  $^{150}\text{Nd}$ , it is not a problem because the  $Q_{\beta\beta}$  value (3367.1 keV) is well above the 2615 keV  $\gamma$ -ray produced in the decay of  $^{208}\text{Tl}$ .

- *Radioactivity measurements for the other components of NEMO 3*

As explained in Section 2.2.3, the Hamamatsu company was chosen to produce the low background PMTs, with very low contamination in all the components (glass, insulator, ceramics, etc). In NEMO 3 the total mass of the PMTs is 239.2 kg for the 3" tubes and 346.5 kg for the 5" tubes, which yield the total activities presented in Table 4.

After selection of the PMTs, the other materials (except shields) were chosen if their total activities in  $^{40}\text{K}$ ,  $^{214}\text{Bi}$  and  $^{208}\text{Tl}$  were at most one tenth of the total activities for the PMTs. It was not always possible to satisfy this criterion for all three contaminants simultaneously. If  $^{40}\text{K}$  exceeds the threshold, the material may have been accepted but not for  $^{214}\text{Bi}$  and  $^{208}\text{Tl}$  which produce background events in the  $Q_{\beta\beta}$  region. In Table 5 the measurements for all selected components of a 5" PMT are summarized. The two last lines of this table provide a comparison between the activity of the selected calorimeter materials and the total activity of the PMTs, the first one being at most of the same order as the PMTs.

Finally, to conclude the NEMO 3 radiopurity report, a summary of the radioactivity measure-

ments is given in Table 6 for the majority of the components of the detector.

### 3. Performance of the detector

#### 3.1. The simulation program

The NEMO 3 simulation program [20] has been developed in the framework of GEANT [21], with the EUCLID industrial software and the EUCLID-GEANT interface [22]. The description of the NEMO 3 device (geometric information, description of more than 60 materials and tracking media) is given with 20 identical sectors, except for the source foils which are placed in their exact positions inside the detector.

The event generator of the program, called GENBB, provides the possibility of generating different double beta decays ( $0\nu$ ,  $2\nu$ , Majorons). Also internal and external background events due to decay of radioactive nuclei may be generated. This event generator also generates the kinematics of special events, such as Compton scattering of external  $\gamma$ -rays or Möller scattering of external electrons, thereby speeding up the computations compared to the simulated events with GEANT.

Important work has been done with the simulation of neutron interactions via the GEANT/MICAP code [23]. This code tracks neutrons from 20 MeV to  $10^{-5}$  eV. It also takes into account  $\gamma$ -ray emission from ( $n, \gamma$ ) captures and ( $n, n'\gamma$ ) scatterings. Using the results of several tests done with a Germanium detector and the NEMO 2 detector [19], the  $\gamma$ -ray generation subroutines were improved by including additional spectroscopic information related to nuclei. Also a new library, GAMLIB, was developed taking into account branching ratios down to as low as 0.1%. This library takes into account the possibility of emission of conversion electrons, which is particularly important for neutron captures with the large internal conversion coefficients observed in many nuclei. A comparison between the simulation and the data with a Am-Be neutron source, using the magnetic field and no shield, is presented in Fig. 10 and shows the excellent agreement for

Table 5  
Radioactivity measurements for 5" PMT components (in mBq/kg)

Sample	Weight (kg)	$^{40}\text{K}$ (mBq/kg)	$^{214}\text{Bi}$ (mBq/kg)	$^{208}\text{Tl}$ (mBq/kg)
Magnetic shield (1.5 mm thick)	1.385	<20	<2	<2
PMMA (light guide + interface)	1.500	<50	<5	<3
Iron ring for light guide	0.555	<35	<3	<3
Light-tightness sleeve	0.191	<80	<17	<12
PMT-Guide glue RTV 615	0.072	$380 \pm 100$	<40	<7
Light-protection glue for PMT				
RTV 106	0.025	$250 \pm 70$	<20	<7
Teflon ribbon (5 layers)	0.023	<170	<20	<5
Guide-Iron ring glue Epotek 310	0.017	<110	<15	<3
Isolated circuit FR2 for PMT divider	0.0105	$320 \pm 100$	$57 \pm 8$	$10 \pm 3$
Light-protection glue RTV 116	0.006	<830	<45	<4
Scintillator-Guide glue BC 600	0.004	<235	<42	<7
Aluminized mylar	0.004	<700	<35	<20
White RTV 160	0.003	$370 \pm 130$	$35 \pm 10$	<4
Capacitor 3.3 nF-2 kV (1 piece)	0.003	<230	<17	$48 \pm 5$
Capacitor 22 nF-250 V (4 pieces)	0.002	<1300	<80	<55
"Radial" solder				
Sn(63%) Pb(37%)	0.002	<400	<50	<30
CMS resistors (23 pieces)	$21 \times 10^{-5}$	<9200	$1400 \pm 500$	<600
Total activity of these components in Bq/PMT		<0.25	<0.028	<0.016
Total activity for one Hamamatsu 5" PMT in Bq/PMT		0.53	0.24	0.014

Total radioactivity of these components is compared to the radioactivity of one PMT (in Bq/PMT).

high energy crossing electron events  $e_{\text{cross}}$  (with  $E_e > 3.2 \text{ MeV}$ ) [24].

In Table 7, the experimental number of ( $e_{\text{cross}}N\gamma$ ) events (with  $N \geq 0$ ) observed per hour without a shield is compared to the expected number of events from simulations. These simulations take into account the  $\gamma$ -ray flux in the laboratory as well as thermal, epithermal and fast neutron fluxes, for which the respective proportions are given in this table. It was assumed that the epithermal neutron flux was equal to the thermal one. The resulting number of ( $2.19 \pm 0.17$ ) observed events is compared to ( $2.05 \pm 0.25$ ) simulated events per hour. The agreement is still very good with the  $\gamma$ -ray shield, which provides an attenuation factor of  $3.2 \pm 0.4$  with a 1200 rejection factor for  $\gamma$ -rays and a 100 one for

thermal neutrons. The number of associated two-electron background events due to the neutron flux, with the  $\gamma$ -ray shield, is  $13.6 \pm 4.4$  for the summed electron energies greater than 2.75 MeV [24]. Recollect that the experiment requires that there be no external background. So there was the addition of the neutron shield, which provides an attenuation factor of 70, which according to the simulation will suppress this background.

### 3.2. Trigger and data acquisition

#### 3.2.1. Acquisition and data file building

Data transfer is achieved via a dedicated Ethernet. The EVB (400 MHz, with a Powerful Ethernet controller) sends data event by event to a PC running Linux. In the transfer, Linux processes

Table 6  
Total radioactivity for the components

Components of NEMO 3	Weight in kg	Total radioactivity (Bq)			
		$^{40}\text{K}$	$^{214}\text{Bi}$	$^{208}\text{Tl}$	$^{60}\text{Co}$
Photomultiplier Tubes	600	831	302	17.8	//
Scintillator blocks	6400	< 102	< 1.2	< 0.6	< 3
Copper	25000	< 125	< 25	< 10	< 6
Iron petals	10000	< 50	< 6	< 8	$17 \pm 4$
$\mu$ -metal PMT shield	2000	< 40	< 4	< 4	< 4
Tracking detector wires	1.7	< $810^{-3}$	< $10^{-3}$	< $610^{-4}$	< $10^{-2}$
Iron shield	180000	< 3000	< 400	< 300	< 600

The PMT activities are lower than the design specification. Moreover, with the exception of the iron shield, all activities are clearly lower than the PMT's.

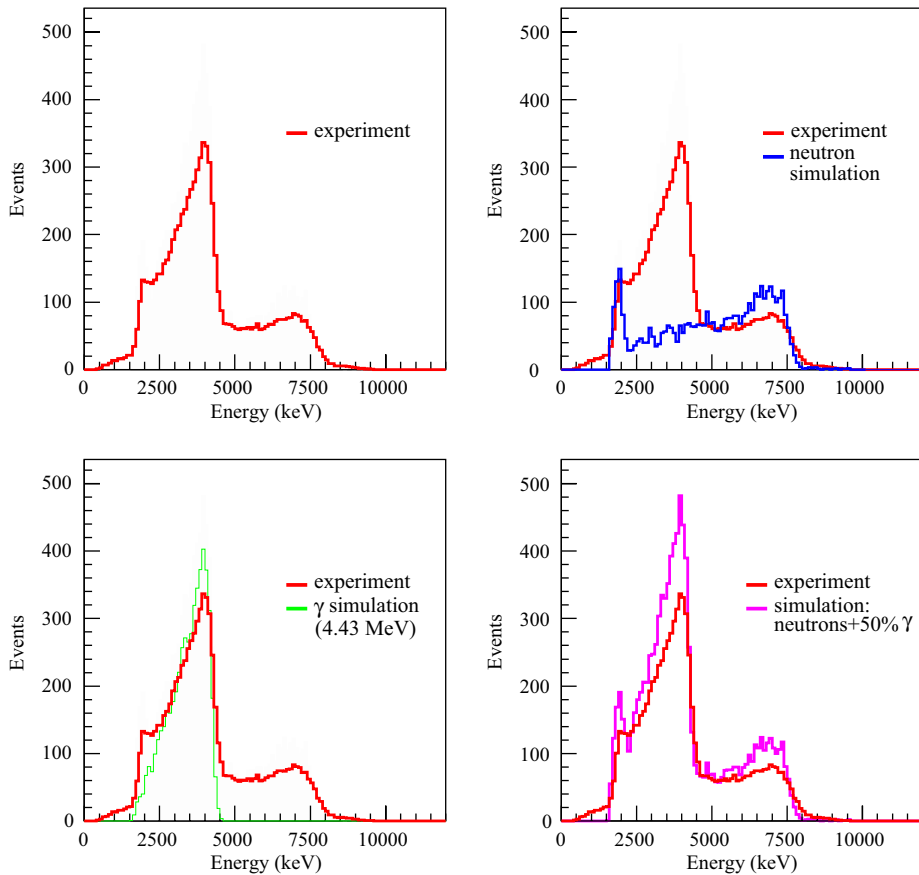


Fig. 10. Comparison between simulation and experimental data with a magnetic field and no shield, for one-crossing-electron events (with and without  $\gamma$ -rays) obtained with a neutron Am–Be source. See text for more details.

Table 7

Comparison between simulated data and experimental data that studies the neutron contamination, without shield (third column) and with the  $\gamma$ -ray shield (fourth column)

Type of events	Simulated flux ( $\times 10^{-6} \text{ s}^{-1} \text{ cm}^{-2}$ )	$e_{\text{cross}} N \gamma$ events in 1 h ( $N \geq 0$ ) ( $E_e > 3.2 \text{ MeV}$ ) without shield	Attenuation factor with $\gamma$ shield
$\gamma$ -rays from laboratory	$3.2 \pm 0.9$	$0.20 \pm 0.05$	1176
Thermal neutrons ( $E \leq 0.1 \text{ eV}$ )	$1.6 \pm 0.1$	$0.50 \pm 0.05$	98
Epithermal neutrons ( $0.1 \text{ eV} < E < 1 \text{ MeV}$ )	$1.6 \pm 0.1$	$0.8 \pm 0.2$	3.2
Fast neutrons ( $E \geq 1 \text{ MeV}$ )	$4 \pm 1$	$0.55 \pm 0.15$	1.1
Simulation total		$2.05 \pm 0.25$	2.7
Experiment total		$2.19 \pm 0.17$	3.2

the data by decoding it and re-organizing it into Random Access ZEBRA files. The initial format of *Cascade* events uses a 12-byte header, followed by calorimeter and Geiger cell information with variable lengths (two bytes per triggered PMT and three bytes per fired cell), and finally a 3-byte trailer. The final format is an “ntuple” format for data analysis. The ntuple building is done on the local acquisition disc and the Zebra file is written every 5000 events.

### 3.2.2. The $\beta\beta$ acquisition

#### • The $\beta\beta$ trigger configuration

The  $\beta\beta$  trigger is the usual one for double beta studies. During the  $\beta\beta$  runs, the trigger configuration (see Section 2.4.3) is the two level one, which enables the readout of events with at least one electron or electron-gamma event. The associated counting rate is between 7.0 and 7.5 Hz depending on the radon level in the laboratory. This configuration has the following properties. At least one triggered scintillator is required with energy deposited greater than 150 keV. Next, a track is reconstructed in a half-sector corresponding to the activation of Geiger cells in at least three of the nine layers and at least two

fired cells in neighbouring layers (using at least two out of the four layers near the source foil, the two intermediate layers, or at least two out of the three layers near the scintillator wall).

The  $\beta\beta$  trigger efficiency was estimated by applying trigger criteria to simulated signal and background events with at least one fired Geiger plane and at least one active PMT. The trigger efficiency check was made with  $\beta\beta 0\nu$  or  $\beta\beta 2\nu$  events from the  $^{100}\text{Mo}$  source foils,  $^{214}\text{Bi}$  and  $^{208}\text{Tl}$  background events from the  $^{100}\text{Mo}$  source foils, and  $^{214}\text{Bi}$  decays in the gas. The number of generated events for each type was 10000. The results are summarized in Table 8, for events with at least one PMT or two PMTs. The proportion of accepted simulated events are given in the first and third columns for at least one and two PMT(s), respectively. The lost events are mainly due to geometrical cuts. The proportion of accepted events after applying the trigger criteria are given in the second and fourth columns. It represents the trigger efficiency (the error bars are statistical uncertainties). The efficiency relative to the number of events with exactly two fired PMTs is the number between squared brackets in the last column. This study shows that trigger criteria do not provide additional cuts and allows one to keep

Table 8

Results of simulations giving trigger efficiencies relative to the number of events coming from  $\beta\beta 0\nu$ ,  $\beta\beta 2\nu$ ,  $^{208}\text{Tl}$  and  $^{214}\text{Bi}$  impurities from Molybdenum source foils and finally  $^{214}\text{Bi}$  impurities from gas

Type of events	Percentage of events with at least one PMT (simulation output)	Associated trigger efficiency (%)	Percentage of events with at least two PMTs (simulation output)	Associated trigger efficiency (%) [see caption]
$\beta\beta 0\nu$ (in Mo foils)	96.1	$96.1 \pm 1.0$	56.8	$56.8 \pm 0.7$ [100]
$\beta\beta 2\nu$ (in Mo foils)	73.6	$73.0 \pm 0.9$	22.7	$22.7 \pm 0.5$ [100]
$^{208}\text{Tl}$ (in Mo foils)	65.7	$63.5 \pm 0.8$	16.9	$16.3 \pm 0.4$ [96.7]
$^{214}\text{Bi}$ (in Mo foils)	58.7	$56.0 \pm 0.8$	13.8	$12.9 \pm 0.4$ [94.0]
$^{214}\text{Bi}$ (in gas)	79.4	$60.0 \pm 0.8$	20.7	$15.4 \pm 0.4$ [74.5]

The number of generated events for each case is 10000.

data for further analysis of all interesting events. The trigger efficiency relative to the number of events with exactly two fired PMTs (criterion for  $\beta\beta$  analysis) are 100% for  $\beta\beta$  events (both  $0\nu$  and  $2\nu$ ), 96.7% and 94% for  $^{214}\text{Bi}$  and  $^{208}\text{Tl}$  in the sources and 74.5% for  $^{214}\text{Bi}$  in the gas.

In the usual trigger conditions, dead time is due both to the  $710\ \mu\text{s}$  delay devoted to the search for alpha particles and to the Geiger readout dead time, which is at least  $587.5\ \mu\text{s}$  for three triggered Geiger cells. For each event the Geiger processor reads the 160 Geiger acquisition cards' status bits and five counters for each fired cell. This is accomplished through a VICbus single read cycle which needs  $2.5\ \mu\text{s}$ . Finally the interrupt handling and Cascade overhead take around  $150\ \mu\text{s}$ . Thus a  $\beta\beta$  event with two triggered PMTs and an average of 16 triggered Geiger cells has a 1.1% dead time of  $1.5\ \text{ms}$  ( $710 + 750\ \mu\text{s}$ ).

#### • Proportion of events in a $\beta\beta$ run

The combination of a tracking volume, delayed tracking electronics, calorimeter and a magnetic field allows NEMO 3 to identify electrons, positrons,  $\gamma$ -rays and  $\alpha$ -particles. The characteristics of events with these particles are outlined below.

- electron (positron): one  $e^-$  ( $e^+$ ) is reconstructed as a track, defined by active Geiger cells in time, with negative (positive) curvature starting from the source foil, passing through the wire chamber and being detected by only one scintillator given that electrons and positrons have a low probability of emitting bremsstrahlung  $\gamma$ -rays, which could trigger neighboring scintillators.
- alpha particle from the source foil: an  $\alpha$ -particle is reconstructed as at least one delayed Geiger cell near an electron or a positron vertex, or as a short straight track defined with delayed hits within  $1.5\ \mu\text{s}$  of each other and passing through a fraction of the wire chamber.
- gamma: a  $\gamma$ -ray corresponds to one or two adjacent scintillators being triggered, without any associated track and without a single Geiger cell hit in front of the scintillator. If there are two active scintillators, they must have been simultaneously triggered, or equivalently their time differences must be lower than the sum of their temporal resolutions.

Fig. 11 shows a typical two electron event coming from a molybdenum source foil ( $\beta\beta 2\nu$  process). In Figs. 12–15 one can see events characteristic of some contamination associated

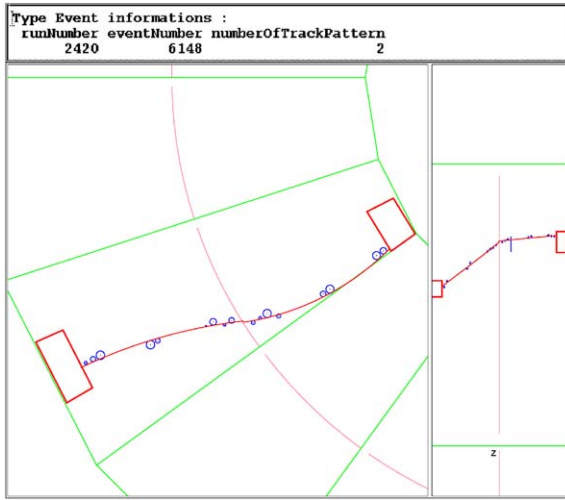


Fig. 11. Two-electron event produced in molybdenum source foil (sector 11). The left portion of this figure shows the transverse top view of NEMO 3, while the right part presents the associated longitudinal view. The circles radii correspond to the transverse distance from the anode wire for each fired cell, they are not error bars. The electrons have energies of 1029 keV (internal wall) and 750 keV (external wall).

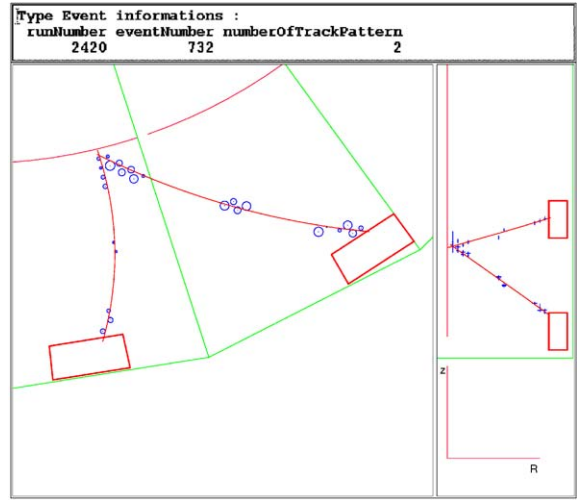


Fig. 13. An  $e^+e^-$  background event produced in a molybdenum foil (sector 15). Note the tracks of opposite curvature.

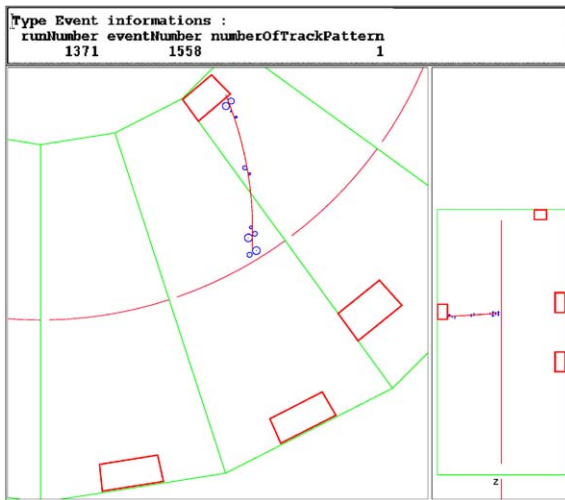


Fig. 12. A  $e^-\gamma\gamma\gamma$  background event produced in a molybdenum foil (sector 16).

with the detector:  $e^-\gamma\gamma\gamma$  event,  $e^+e^-$  pair production,  $e^-\alpha$  event and a high energy crossing electron.

The proportion of different types of events in a  $\beta\beta$  run is given in Table 9. Note that  $\beta\beta$ -like events

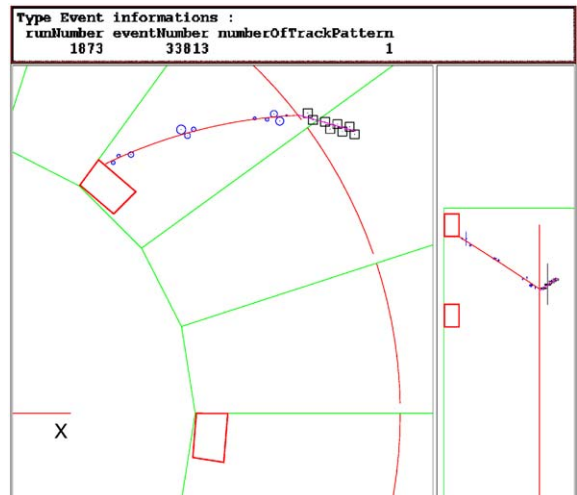


Fig. 14. Decay of some internal contamination producing a single electron event coming from a molybdenum source foil (sector 02) followed by a delayed alpha particle, which is the short straight track represented by open squares. Note the presence of one gamma-ray.

represent 0.15% of the registered events, which means one  $\beta\beta$ -like event occurs every 1.5 min.

### 3.2.3. Other acquisition types

With the same trigger configuration, one can have higher counting rates and lower dead times



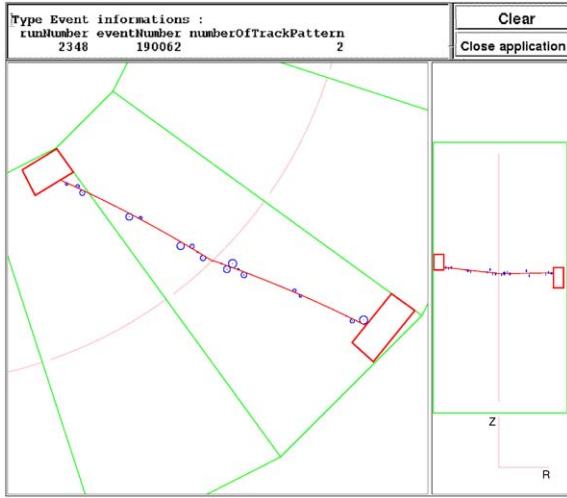


Fig. 15. Example of an external source of background: it is a view of high energy crossing electron, which is most likely produced by a  $\gamma$ -ray emitted after a neutron capture in the copper frame. This type of events is used to establish reconstruction formulae for transverse and longitudinal positions in the tracking detector. It can be distinguished from back-to-back source foil events by time-of-flight measurements (see Section 3.4).

using acquisition processes without looking for delayed events. It is however impossible to remove the 710  $\mu$ s fixed delay, but the Geiger readout can begin with the calorimeter interrupt. In this case the busy Geiger and the busy calorimeter are superimposed and the overlap is reduced to about 200  $\mu$ s, which gives a dead time of  $\sim 1$  ms.

It is possible to take data with just the calorimeter or just the tracking detector. For laser runs, the counting rate is 250 Hz, with 10 Hz/PMT of that being the laser data, and the remainder coming from  $^{207}\text{Bi}$  in the six reference counters.

Calibration runs with 60  $^{207}\text{Bi}$  sources use a  $\beta\beta$  trigger, with an acquisition rate of 240 Hz. Other calibration runs use only calorimeter acquisition, with a special one developed for  $^{90}\text{Sr}$  to determine the beta end-point. The acquisition of only the energy spectra is realized without ntuple building for the whole calorimeter, which permits very high counting rates (up to 30 kHz) with the smaller output files of 32 Mbytes. All of the 32 Mbytes of the calorimeter processor are used to construct histograms.

Table 9

The proportions of events which are used for  $\beta\beta$  and background analyses (see Table 10 for the associated trigger), for which  $1e^-$  or  $1e^+$  events are reconstructed with a single track between the source foil and an associated PMT on one side of the detector

Type of event	Proportion (in %)
$1e^-$ , no $\gamma$ -ray	7.7
$1e^-$ , $N\gamma$ -rays, $N \geq 1$	2.0
$1e^+$ , no $\gamma$ -ray	1.4
$1e^+$ , $N\gamma$ -rays, $N \geq 1$	0.66
$e^+e^-$ pairs	1.5
One-crossing-electron	1.1
Two-electron events, no $\gamma$ -ray	0.15

$\sim 90\%$  of the events do not pass the cuts because the trigger imposes very loose constraints so most of the events have only a few triggered cells which are not sufficient to reconstruct tracks or correspond to events reconstructed with more than one track on one side of the detector. These last events are due to electron backscattering at the scintillators or other mechanisms such as the magnetic field turning electrons back towards the source foil. Note that  $e^+e^-$  or  $e^-e^-$  events created in the source foils and one-crossing-electron events are reconstructed with two single tracks.

Counting rates associated with different triggers and acquisition types are presented in Table 10.

### 3.3. Tracking detector performance

#### 3.3.1. Final operating conditions of the tracking detector

Since February 2003, with the new gas mixture, the longitudinal propagation velocity is 5.2 cm/ $\mu$ s corresponding to a full propagation time  $\langle t_{LC} + t_{HC} \rangle \sim 50 \mu$ s and 90% of Geiger cells have a longitudinal propagation efficiency greater than 95%. The single counting rate per cell is  $\sim 0.2$  Hz.

There were eventually only 30 channels of the 6180 ( $<0.5\%$ ) with missing anode signals, of which there were four cells disconnected due to anode wires in contact with ground wires, eight cells due to interconnection problems, and 18 hot cells<sup>13</sup> ( $\sim 0.3\%$ ). The number of Geiger cells with at least one missing cathode signal were 160 (2.6%), due again to interconnection problems.

<sup>13</sup>Self-discharging Geiger cell.

Table 10  
Different counting rates for different types of trigger

Type of run	Trigger conditions	Event type	Counting rate (Hz)
$\beta\beta$ run	$\geq 1$ triggered PMT + 1 track with $E_{\text{PMT}} > 150$ keV and at least 3 fired Geiger cells	(e), (e, e), (e, $N\gamma$ ), (e, e, $N\gamma$ ), with $N \geq 1$	7.0–7.5
Calo run	$\geq 1$ triggered PMT with $E_{\text{PMT}} > 150$ keV	PMT singles	580
Geiger run	$\geq 1$ track	GG singles	65
Special calibration run	$\geq 2$ triggered PMTs + 1 track with $E_{\text{PMTs}} > 150$ keV and at least 3 fired Geiger cells	(e, e), (e, $N\gamma$ ), (e, e, $N\gamma$ ), with $N \geq 1$	1.15

### 3.3.2. Geiger TDC analysis

As discussed in Section 2.4 there are four variables associated with the Geiger TDCs. They are  $tdc_{\text{LC}}$  and  $tdc_{\text{HC}}$  for the two cathode ring times,  $tdc_{\text{A}}$  for the anode time and  $tdc_{\alpha}$  for the delayed time (see Eqs. 6–9). The triggered Geiger cells are classified into different types according to the values of these four TDC signals. There are “in-time hits” coming from electron or positron tracks. Also “delayed hits” are delayed triggers of cells used to study  $\alpha$ -particle events. Finally there are “refired cells” which are active because of cross-talk (cells fired by a neighboring in-time cell) and “noisy cells”.

### 3.3.3. Track reconstruction

#### • Principle

Geiger events are first tagged with one of the four previously defined criteria. The refired and noisy cells are rejected, with about one or two refired cells per event. The number of noisy cells is typically negligible. Then, two different pattern recognition and track fit procedures are carried out, one for in-time hits and the other for delayed hits.

For in-time hits the pattern recognition and tracking are carried out using a cellular automaton algorithm, which was previously used for NEMO 2 tracking [25]. The NEMO 3 algorithm uses a set of consecutive segments which connect pairs of active cells in neighboring layers. A candidate

track is defined and characterized by the number of segments (length of the track) and the sum of the angles between the segments. In NEMO 3, the longest track is favored. The curvature of the track depends on the magnetic field. A new track search is then begun with the other segments until there are not enough segments remaining to construct a track.

Concerning the track fitting procedure, there are two successive fits in order to solve the left/right ambiguities in the transverse plane.

Each reconstructed track is extrapolated to the source foil and a vertex position is calculated whose transverse and longitudinal coordinates are  $R\phi$  and  $Z$ , with an origin  $Z = 0$  at the half-height position of the source foils (see Section 3.3.6). The track is also projected onto an associated scintillator surface and the calculated coordinates of the scintillator are  $R_S\phi_S$  and  $Z_S$ , where  $R_S$  is the transversal distance between the detector’s center and the entrance surface of the scintillator.

For delayed hits the treatment in the longitudinal plane is the same as that for in-time hits. The treatment in the transverse plane is slightly modified since there are only relative drift time measurements. Delayed hits can form a track only if the differences in anode times are shorter than  $1.5 \mu\text{s}$ , which is approximately the maximum drift time in a Geiger cell. For each hit, the drift distance is computed from the  $tdc_{\alpha}$  for the cell, assuming the delayed hit with the higher  $tdc_{\alpha}$  value corresponds to a particle passing through the anode wire of the cell.

- *Association between tracks and energy deposited in the calorimeters*

An electron or positron event needs track associated with a scintillator. This is accomplished if there is at least one hit in the two Geiger cell layers nearest to the scintillators which belongs to the track. Additionally, geometrical cuts are applied which extrapolate the position of the track to the surface of the scintillator ( $R_S\phi_S$  and  $Z_S$ ) which has to be located less than 3 cm away from the edges of the scintillator.

### 3.3.4. Reconstruction of the particle position in the cell

Studies with a laser and a nine cell prototype of the tracking detector were carried out to establish formulae giving transverse ( $r_\perp$ ) and longitudinal ( $z$ ) positions in a cell from anode drift times and both cathode times [26]. These formulae have been improved with NEMO 3 [27], using data taken with high energy crossing electrons ( $>4.5$  MeV). These electrons were created by an intense Am–Be source producing fast neutrons with an activity of around  $2.2 \times 10^5$  n/s. Fast neutrons are thermalized in the scintillators; then high energy  $\gamma$ -rays are created by the capture of the neutrons in the copper walls, producing one-crossing-electron events by the Compton effect. With high energy crossing electrons and with an energy deposited  $>3$  MeV in the second scintillator, the multiple scattering is found to be negligible and the track is well defined.

The track resulting from the fit is assumed to be identical to the real track. Thus, the transverse and longitudinal reconstruction formulae are obtained by comparing the distance to the identified track with the drift anode time and the two cathode times.

- *Transverse position in the cell*

Fig. 16 shows the transverse distance  $r_\perp$  to the track as a function of the anode time  $t_A$ . Near the wire (between 1 and 4.5 mm), the drift velocity corresponds to the saturation regime and is  $2.3$  cm/ $\mu$ s. Far from the anode wire, the drift speed is proportional to the electric field. Thus, for

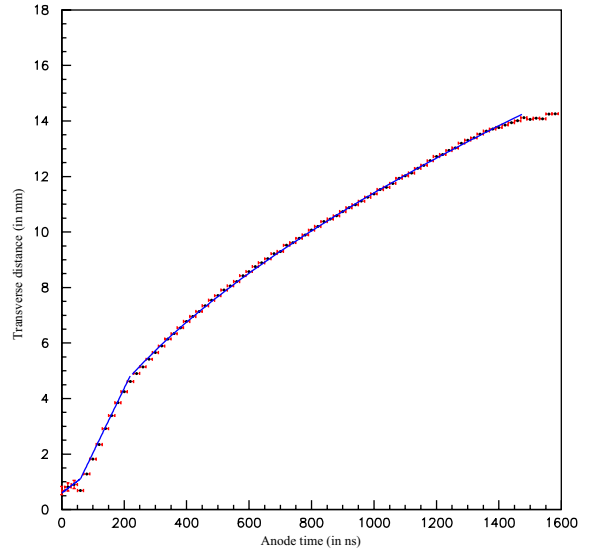


Fig. 16. Transverse distance to a constructed track  $r_\perp$  (in mm) as a function of anode time  $t_A$  (in ns) obtained with high energy crossing events ( $e_{\text{cross}} > 4.5$  MeV).

$220 < t_A < 1480$  ns, the electric field is proportional to  $1/r$ , which leads to a transversal distance proportional to  $\sqrt{t_A}$ .

- *Longitudinal position in the cell*

According to the two measured cathode times  $t_{LC}$  and  $t_{HC}$ , and using the origin of the  $z$ -axis fixed at the half-height of the cells, the longitudinal position  $z$  is given, in mm, by:

$$z = \frac{L_{\text{eff}}}{2} \frac{t_{HC} - t_{LC}}{t_{LC} + t_{HC}} \left[ 1 - 0.505 \cdot 10^{-4} \frac{L_{\text{eff}}}{2} \times \left( 1 - \frac{|t_{HC} - t_{LC}|}{t_{LC} + t_{HC}} \right) \right]$$

where  $L_{\text{eff}} = 2607$  mm is the effective length of the cell, which is lower than the full cell length of 2700 mm that includes the two rings (each is 30 mm long). This effective length is a consequence of the fact that cathode signals exceed their threshold a few centimeters before the plasma reaches the cathode ring. The  $L_{\text{eff}}$  value depends on the HV and gas mixture.

The first-order term corresponds to a constant propagation speed for the plasma. In this case, the longitudinal position is simply the propagation

time of the plasma to the nearest ring, divided by the propagation velocity.

The second-order term is a correction, which takes into account the reduced propagation velocity due to a decrease in the high voltage during the plasma propagation (this factor also depends on the HV and gas mixture). The correction has a maximum value of around 20 mm in two positions corresponding, respectively, to 25% and 75% of the cell length.

If one of the two cathode times is missing, the relation remains the same, but only for the TDC with a non-zero value. The other cathode time is obtained using an average plasma propagation velocity. The  $z$  position in the Geiger cell is then reconstructed using the same formula as above. The propagation velocity has to be calculated and stored in the database for each Geiger cell. If both cathode times are missing, no reconstruction of the  $z$  position of the Geiger cell hit is possible.

- *Transverse and longitudinal resolution of the Geiger cells [27]*

The residual distribution in the transverse direction is obtained by plotting the distance between the accepted track and the reconstructed position of the Geiger cell hit, using high energy crossing electrons. The full-width at half-maximum (FWHM) of the spectrum is used to compute the transverse resolution of the cells as  $\sigma_{\perp} = \text{FWHM}/2.35$ . The average value of this resolution is:

$$\sigma_{\perp} = 0.5 \text{ mm.}$$

Note that  $\sigma_{\perp}/R \sim 3\%$ , where  $R$  is the radius of the cell (15 mm). In order to estimate the contribution of multiple scattering, a study of the transverse resolution was carried out as a function of the variable  $\sqrt{L_{\text{track}}}/E$ , where  $L_{\text{track}}$  is the track length and  $E$  is the initial energy of the electron in keV (see Fig. 17). The associated relation, which shows the resolution dependence with multiple scattering, is:

$$\sigma_{\perp} = \sqrt{\sigma_{\text{int}}^2 + k \left( \frac{\sqrt{L_{\text{track}}}}{E} \right)^2}$$

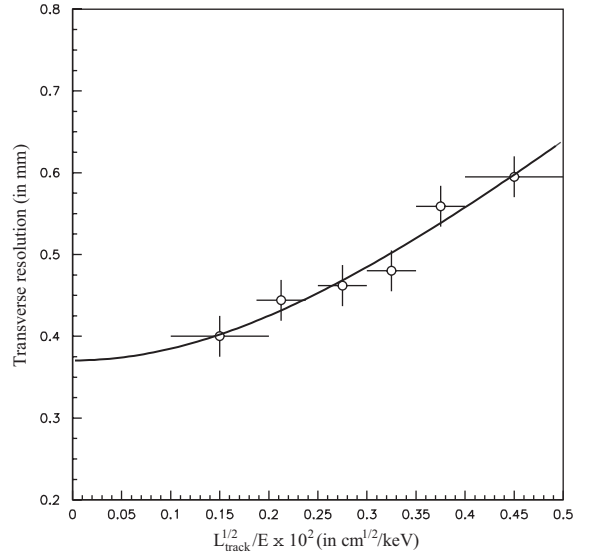


Fig. 17. Distribution of transverse resolution per cell  $\sigma_{\perp}$  (in cm) as a function of the variable  $\sqrt{L_{\text{track}}}/E$ . The associated curve is the result of the fit given by  $\sigma_{\perp} = \sqrt{\sigma_{\text{int}}^2 + k(\sqrt{L_{\text{track}}}/E)^2}$ .

where the intrinsic resolution is given by  $\sigma_{\text{int}} = (0.37 \pm 0.02)$  mm and  $k = (10.8 \pm 1.7)$  mm keV<sup>2</sup> is a constant.

The longitudinal resolution of the cells is obtained by the same method applied in the longitudinal plane, here the average value is

$$\sigma_{\parallel} = 0.8 \text{ cm.}$$

Note that  $\sigma_{\parallel}/L_{\text{cell}} \sim 3\%$ , where  $L_{\text{cell}}$  is the length of the cell. Fig. 18 shows the influence of the dip angle  $\theta$  on the longitudinal resolution. Here  $\sigma_{\parallel}$  is multiplied by a factor of two for an electron crossing the wire at an angle  $\theta = 45^\circ$  compared to a track perpendicular to the wire. This increase is due to the longitudinal spread of the primary ionization electrons along the anode wire. Fig. 19 shows the longitudinal resolution  $\sigma_{\parallel}$  as a function of the longitudinal position  $z$ . The associated relation is:

$$\sigma_{\parallel} = \sigma_0 \sqrt{1 - \left( \frac{z}{L_{\text{eff}}/2} \right)^2}$$

where  $\sigma_0 = (1.050 \pm 0.008)$  cm is the maximum resolution at the center of the detector;  $L_{\text{eff}}$  is the

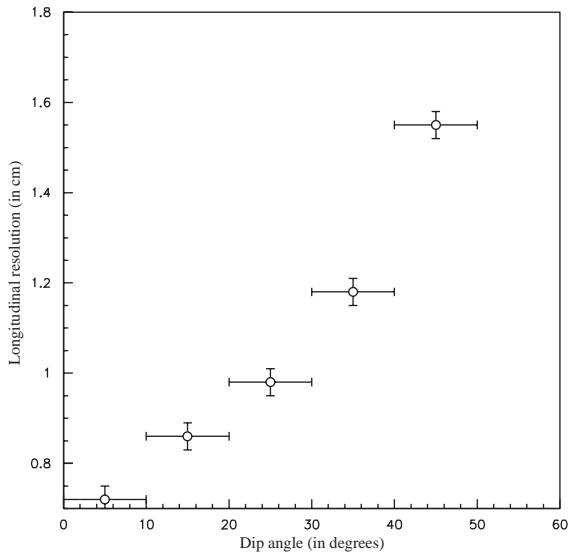


Fig. 18. Distribution of longitudinal resolution in a cell  $\sigma_{\parallel}$  (in cm) as a function of the dip angle  $\theta$  (in degrees).

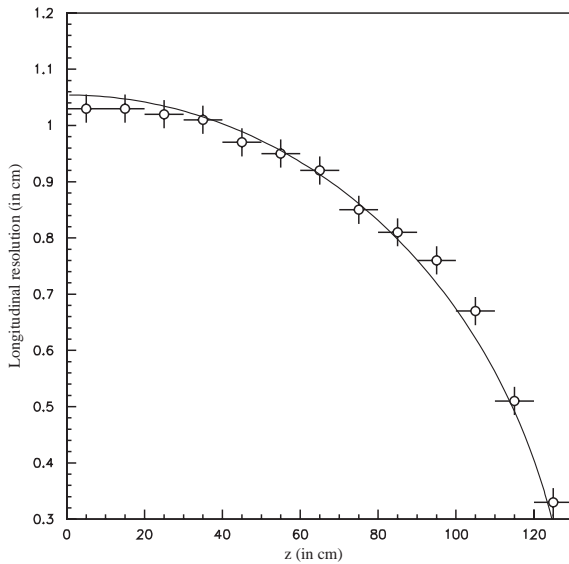


Fig. 19. Distribution of the longitudinal resolution in a cell  $\sigma_{\parallel}$  (in cm) as a function of longitudinal position  $z$  (in cm). The associated curve is the result of the fit given by  $\sigma_{\parallel} = \sigma_0 \sqrt{1 - (2z/L_{\text{eff}})^2}$ .

effective length as defined above. This form is characteristic of the statistical fluctuations in the number of avalanches occurring during the longitudinal propagation.

### 3.3.5. Misidentification of electrons and positrons [27]

There is a possible misidentification of electrons and positrons in tests with high energy ( $\geq 3$  MeV) crossing electrons which are produced during neutron source studies. These crossing events are dominated ( $>99\%$ ) by electrons and are reconstructed as two half-sector electron-type events with successive negative curvature. The first half from an external scintillator to the source foil on one side of the foil, the second one from the source foil to an internal scintillator, both with a common vertex on the foil. Thus it is possible to check the probability of mistaking a positive curvature positron event against an electron event after the foil. The associated distribution of the rate of error as a function of the electron energy is presented in Fig. 20. The  $e^+e^-$  misidentification is around 3% at 1 MeV using extrapolated results.

### 3.3.6. The vertex reconstruction [27]

- Principle

The quality of vertex reconstruction has been analyzed by taking data with 60  $^{207}\text{Bi}$  sources

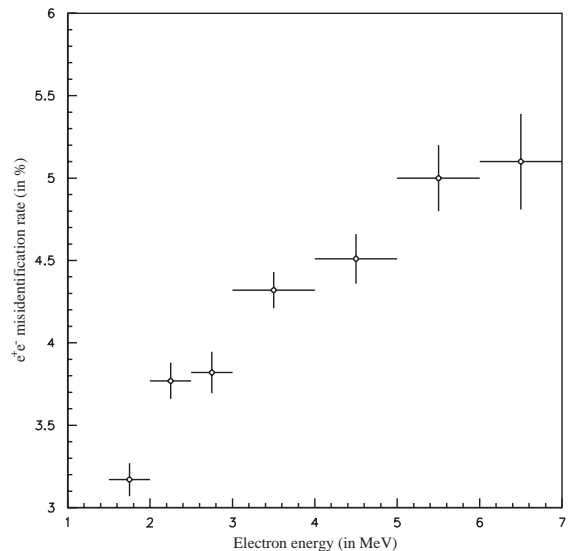


Fig. 20. Distribution of  $e^+e^-$  misidentification rate as a function of electron energy.

placed in the three positions (T for Top with  $Z = 90$  cm, C for Center with  $Z = 0$  cm, and B for Bottom with  $Z = -90$  cm) on each sector inside the calibration tubes. The  $R\phi$  and  $Z$  positions of these sources (see Section 3.3.3) are known with an accuracy of 1 mm.  $\phi$  is the polar angle, using cylindrical coordinates, with an origin at sector 0;  $R = 155.5$  cm is the transversal distance between the detector's center and the source foils; for sector 00, the  $R\phi$  value for the calibration source position is  $(148.6 \pm 0.1)$  cm and there is a step of  $18^\circ$  to obtain  $R\phi$  for each subsequent sector.

Conversion electron events coming from these sources are selected, with energies of 482 or 976 keV. The distribution of the 60 reconstructed vertices are presented in Fig. 21. With this sample of data the differences between reconstructed and expected vertex positions can be estimated. The difference in the transverse plane is defined as  $\Delta R\phi = R\phi_{\text{rec}} - R\phi_{\text{exp}}$  and in the longitudinal plane as  $\Delta Z = Z_{\text{rec}} - Z_{\text{exp}}$ .

For transverse reconstruction of the vertex, the average position shifts between reconstructed and expected vertices are the same for the three source

positions (T, C and B):

$$\langle \Delta R\phi \rangle = 1.6 \text{ mm.}$$

These  $\langle \Delta R\phi \rangle$  are compatible with the accuracy of the mechanical  $R\phi$  positions of the calibration sources and calibration tubes.

The average differences in the longitudinal reconstruction for the three positions are the following:

$$\langle \Delta Z(T) \rangle = -3.25 \pm 0.03 \text{ mm}$$

$$\langle \Delta Z(C) \rangle = -1.64 \pm 0.07 \text{ mm}$$

$$\langle \Delta Z(B) \rangle = -0.52 \pm 0.03 \text{ mm.}$$

Note the maximum value of  $\langle \Delta Z \rangle$  is lower than the longitudinal vertex resolution. The longitudinal position of the vertex is independent of the angle. However, an asymmetry for the three positions is observed, which corresponds to an error of around 20 ns on the cathode time measurement. It can be explained by the fact that the same discrimination threshold was used for both cathode signals although the high cathode signal is lower.

#### • Vertex resolution

The *transverse resolution*  $\sigma_{R\phi}$  depends on the energy of the track. Using the two conversion electron energy values ( $\sim 0.5$  MeV and  $\sim 1$  MeV), it is possible to determine average values for these resolutions:

$$\sigma_{R\phi}(0.5 \text{ MeV}) = 0.3 \text{ cm} \quad \text{and}$$

$$\sigma_{R\phi}(1 \text{ MeV}) = 0.2 \text{ cm.}$$

The *longitudinal resolution*  $\sigma_Z$  depends on both energy and position. Using 1 MeV electrons, the same value of  $\sigma_Z = 0.7$  cm was obtained for both T and B positions and  $\sigma_Z = 0.9$  cm was obtained for the C position. For 0.5 MeV electrons, the longitudinal resolution is  $\sigma_Z = 1.1$  cm on average for the T and B positions and 1.3 cm for the C position.

There is another dependence on the dip angle  $\theta$  (see Fig. 22), which obeys the relation:

$$\sigma_Z = \frac{\sigma'_0}{\cos \theta}$$

where, on average,  $\sigma'_0 = (0.632 \pm 0.004)$  cm for the T position,  $\sigma'_0 = (0.825 \pm 0.006)$  cm for the C

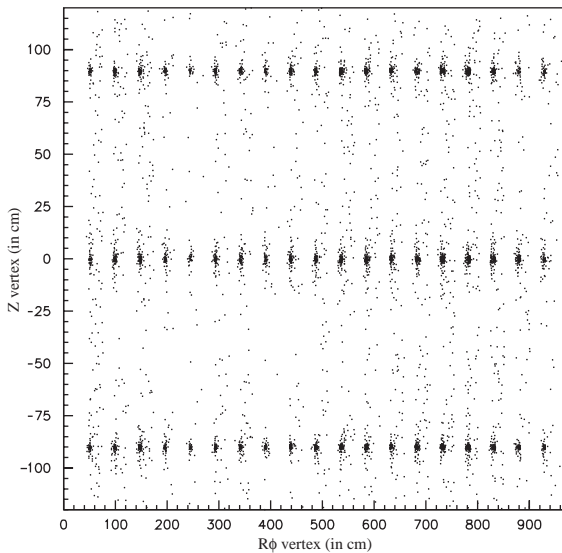


Fig. 21. Distribution of reconstructed vertices for the 60 positions of the calibration  $^{207}\text{Bi}$  sources, in the one-electron channel.

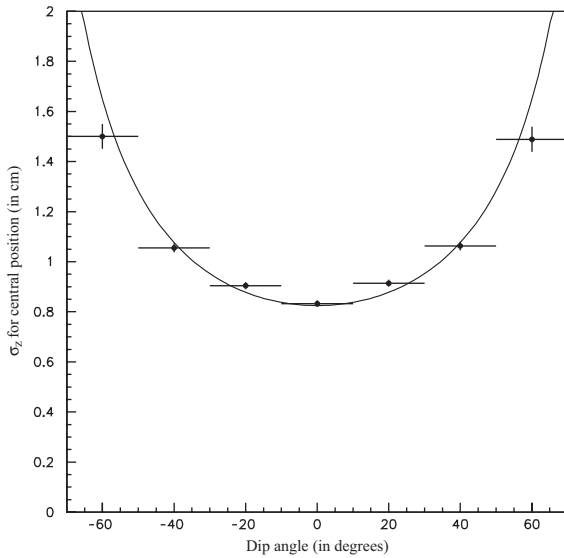


Fig. 22. Distribution of the vertex longitudinal resolution  $\sigma_z$  (in cm) as a function of the dip angle  $\theta$  (in degrees), with a  $\sigma'_0/\cos\theta$  adjustment (obtained with  $^{207}\text{Bi}$  sources located in the central position).

position and  $\sigma'_0 = (0.615 \pm 0.004)\text{cm}$  for the B position.

- *Study with two electrons events*

The  $\beta\beta$  analysis reconstructs events with two tracks coming from the same vertex. Thus, it is important to study the vertex resolution of the two electron channel in order to check the measured transverse and longitudinal dispersions. These dispersions,  $\delta R\phi$  and  $\delta Z$ , are defined as the distance between the vertices associated with the two reconstructed tracks.

Using events coming from the 60  $^{207}\text{Bi}$  sources with two simultaneous electrons (intensity of  $\sim 2\%$ ), one builds  $\delta R\phi$  and  $\delta Z$  distributions, which produce the resolutions:

$$\sigma(\delta R\phi) = 0.6\text{ cm} \quad \text{and} \quad \sigma(\delta Z) = 1.0\text{ cm}$$

It is also true that  $\sigma(\delta R\phi) = 0.1\text{ cm}$ , if one constrains the two tracks to have a common vertex. These resolutions allow one to make a distinction between two strips in a source foil in a given sector, which is crucial for sectors composed of different sources.

### 3.4. Operating conditions of the calorimeter

#### 3.4.1. Working performance of the calorimeter

The operating voltages of the PMTs are 1800 V for the 3" and 1350 V for the 5" PMTs. The single counting rate is  $\sim 0.2\text{ Hz/PMT}$  above a 48 mV threshold ( $\sim 150\text{ keV}$ ). In total, 98% of the PMTs are functioning to design specifications.

#### 3.4.2. Energy resolution of the counters

- *Energy calibration results*

As explained in Section 2.5, special calibration runs are used to obtain the three points on the energy versus ADC channel line. Two results of multi-gaussian fits (K, L, M electrons) to the peak positions in the  $^{207}\text{Bi}$  data (see Fig. 23), and one from the beta end-point energy from  $^{90}\text{Sr}$  data (see Fig. 24).

The calibration lines obtained from the two  $^{207}\text{Bi}$  peaks as well as the fit combining  $^{207}\text{Bi}$  and  $^{90}\text{Sr}$  results do not necessarily intersect the origin of the axes. This effect was previously observed with data obtained with an electron spectrometer and in other experiments. A typical example is given in Fig. 25.

It was first discovered with calibration data that the response of a counter depends upon the entrance point of the electron, with a weak dependence of 1–2% for counters equipped with 3" PMTs and a stronger dependence of up to 10% for those equipped with 5" PMTs. This effect has a non-negligible consequence on the energy resolution, thus one has to correct it for the seven different types of counters, L1–L4 for petal scintillators and EE, EC and IN for wall scintillators (see Table 11). One can see that these resolutions depend primarily on the type of PMT associated with the scintillator which on average are 6.1% for the 5" PMTs and 7.3% for the 3" PMTs.

#### 3.4.3. Timing resolution of the counters

- *Timing corrections*

As explained in Section 2.5, the relative timing offset  $\varepsilon^{(i)}$  for each counter  $i$  is determined using

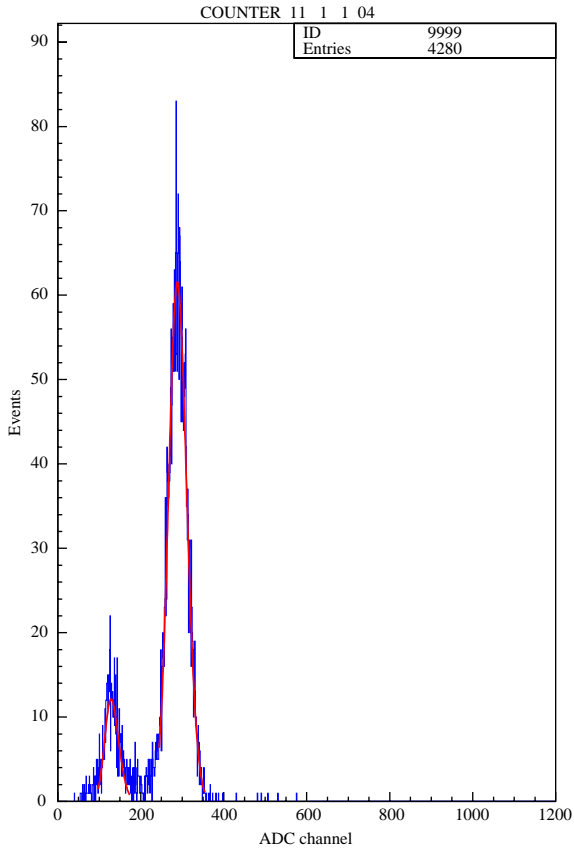


Fig. 23. Spectral fit of the 482 and 976 keV  $\gamma$ -rays coming from  $^{207}\text{Bi}$  decays for one counter ( $\sim 3$  keV/channel).

different calibration sources, in order to provide the time alignment of the calorimeter.

The two-gamma events from  $^{60}\text{Co}$  sources are used for time alignment with  $\gamma$ -rays. The distribution of the arrival time difference in the counters before and after alignment is shown in Fig. 26. The distribution after alignment has a resulting RMS of  $\sim 660$  ps for gamma events.

The two-electron events from  $^{207}\text{Bi}$  sources are used for time alignment with electrons and to obtain the time resolution as a function of electron energy as shown in Fig. 27. This resolution is around 250 ps for 1 MeV electrons.

The energy dependence of the timing signal is adjusted by a four parameter formula, as shown in Eq. (13). The first method to find this dependence is to use a “complete” laser run. A second is to use

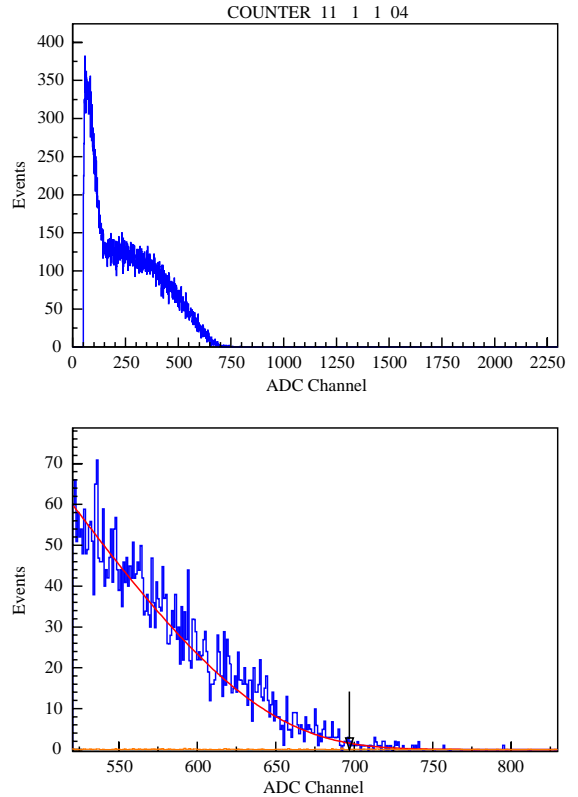


Fig. 24. An example of beta-decay end-point adjustment (2.283 MeV) in the energy spectrum associated with  $^{90}\text{Sr}$  calibration sources ( $\sim 3$  keV/channel). The top of the figure shows the full spectrum and the bottom shows the fit to the high-energy tail of the spectrum, which is made with a function describing the shape of a single  $\beta$  spectrum of  $^{90}\text{Y}$ , convolved with the energy resolution function  $\sigma(E)$  and taking into account the mean energy loss of the electrons.

the two-electron events from  $^{207}\text{Bi}$  sources. The results of this second method for the different types of scintillators are plotted in Fig. 28.

- *The time-of-flight (TOF) selection criterion*

To distinguish between one-crossing-electron events from external background and two-electron events from the source foil, the same TOF rejection criterion is applied that was used in the NEMO 2 experiment [4]. It is based on the comparison between the measured ( $\Delta T_{\text{meas}}$ ) and the calculated ( $\Delta T_{\text{cal}}$ ) time differences of the scintillator hits. A single electron crosses the



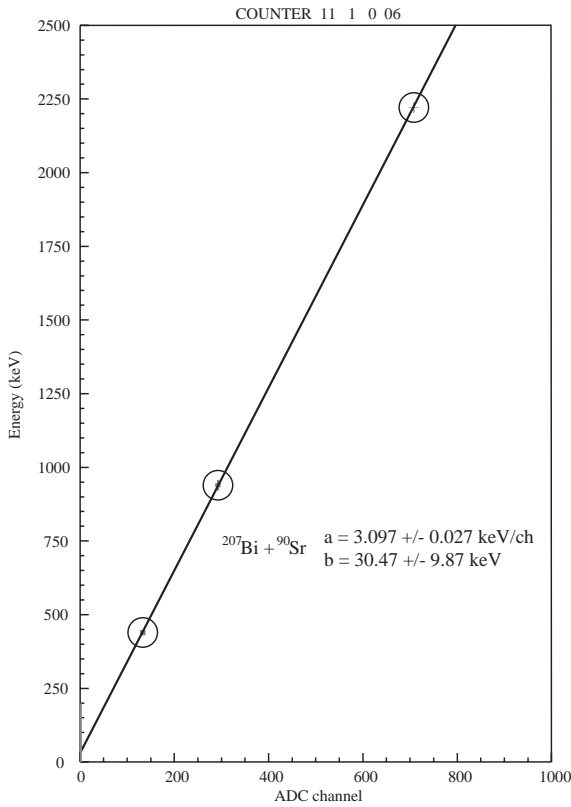


Fig. 25. An example of the energy calibration using 3 points coming from  $^{207}\text{Bi}$  and  $^{90}\text{Sr}$  data. The calibration parameters ( $a$  and  $b$ ) of the energy-channel relation are obtained this way for each counter ( $\sim 3 \text{ keV/channel}$ ).

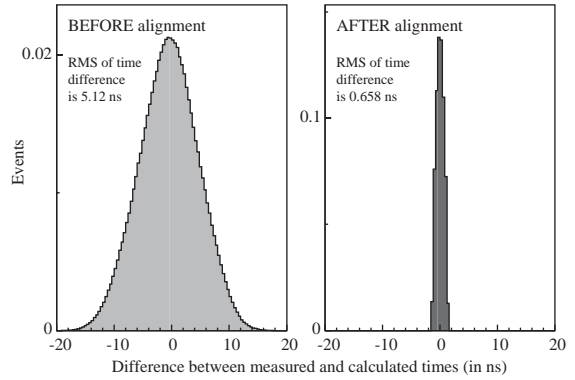


Fig. 26. Distribution of the arrival time difference in the counters before and after alignment with  $^{60}\text{Co}$  calibration sources. The distribution after alignment has an RMS of  $\sim 660 \text{ ps}$  (obtained with two-gamma events).

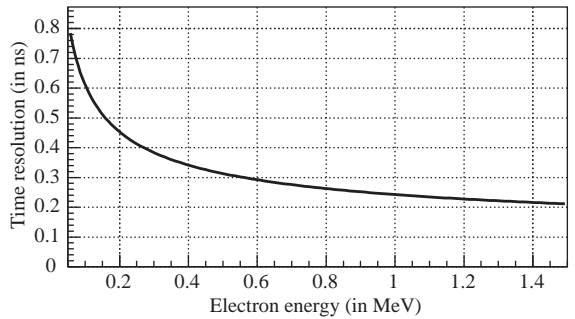


Fig. 27. Time resolution (in ns) as a function of the electron energy (in MeV), obtained with two-electron events.

Table 11  
Energy resolutions corrected from entrance position on scintillators

Block type	Associated PMT	Corrected resolution $\sigma_E/E$ at 1 MeV (in %)
IN	3"	$7.3 \pm 0.1$
EC	5"	$6.0 \pm 0.1$
EE	5"	$6.0 \pm 0.1$
L1	3"	$7.1 \pm 0.2$
L2	3"	$7.1 \pm 0.2$
L3	3"	$7.5 \pm 0.2$
L4	5"	$6.3 \pm 0.2$

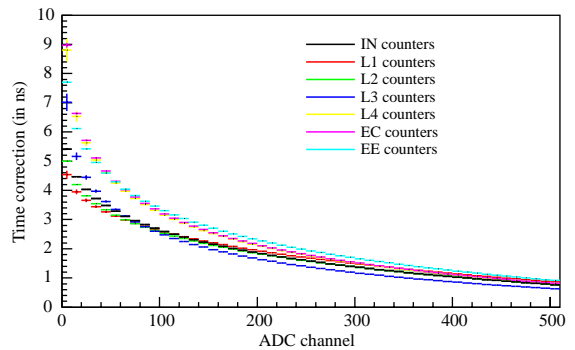


Fig. 28. Time correction (in ns) as a function of the ADC channel for different types of counters ( $\sim 3 \text{ keV/channel}$ ).

detector in a time  $(\Delta T_{\text{cal}})_{\text{ext}}$  and two electrons emitted from the source foil lead to a calculated TOF equal to  $(\Delta T_{\text{cal}})_{\text{int}}$ .

Fig. 29 represents  $(\Delta T_{\text{meas}} - \Delta T_{\text{cal}})_{\text{int}}$  (for internal hypothesis) vs.  $(\Delta T_{\text{meas}} - \Delta T_{\text{cal}})_{\text{ext}}$  (for external hypothesis) for selected two track events (except TOF criterium) from  $^{100}\text{Mo}$  foils. The two-electron events coming from the source foil are centered around  $(\Delta T_{\text{meas}} - \Delta T_{\text{cal}})_{\text{int}} \sim 0$  ns whereas the one-crossing-electron events have  $(\Delta T_{\text{meas}} - \Delta T_{\text{cal}})_{\text{int}} \sim \pm 5$  ns in the internal hypothesis. The calculated TOFs are based on the particle energy deposits in the scintillator counters. Thus,

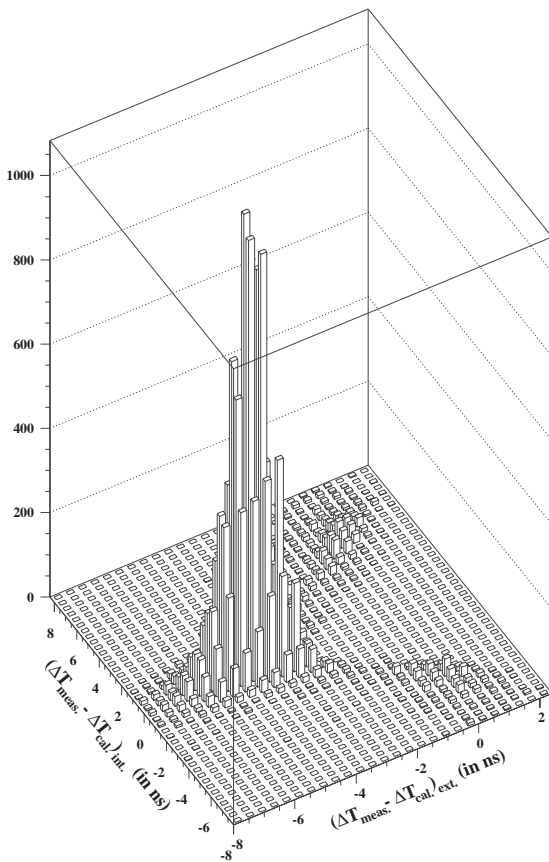


Fig. 29.  $(\Delta T_{\text{meas}} - \Delta T_{\text{cal}})_{\text{int}}$  vs.  $(\Delta T_{\text{meas}} - \Delta T_{\text{cal}})_{\text{ext}}$  for two-track events from  $^{100}\text{Mo}$  source foils. The events located in the highest peak along the line  $(\Delta T_{\text{meas}} - \Delta T_{\text{cal}})_{\text{int}} = 0$  ns (internal hypothesis) are produced in the source foils; those present in the two secondary bumps on the line  $(\Delta T_{\text{meas}} - \Delta T_{\text{cal}})_{\text{ext}} \sim 0$  ns (external hypothesis) result from electrons crossing the detector. See text for more details.

in the case of a through-going electron the calculation of  $(\Delta T_{\text{meas}} - \Delta T_{\text{cal}})_{\text{int}}$  relies on a wrong estimate of the time (calculated from a hypothesis using the energy) of one of the tracks and results in a large (around 5 ns) positive or negative value for the TOF as it can be observed in Fig. 29, which shows well-separated bumps.

#### 3.4.4. Counter stability

For each counter, there are stability corrections which are calculated using the absolute calibration obtained with sources as a reference and laser spectra. These corrections take into account any variation of the laser, which is monitored by reference PMTs. This variation measurement is determined by comparing the laser peak position and the 976 keV peak position from the  $^{207}\text{Bi}$  for the six reference counters (see Section 2.5.6).

An example of a long term (one month) survey of the energy correction parameter ( $e_{\text{corr}}$ ) for one counter is shown in Fig. 30. This stable behaviour with gain variations of less than 2% is consistent with 90% of the counters with 5" PMTs and 96% with 3" PMTs. These corrections are stored in the database and used with  $\beta\beta$  runs to calculate particle energies.

## 4. Conclusion

The NEMO 3 experiment is based on the direct detection of the two electrons emitted from double

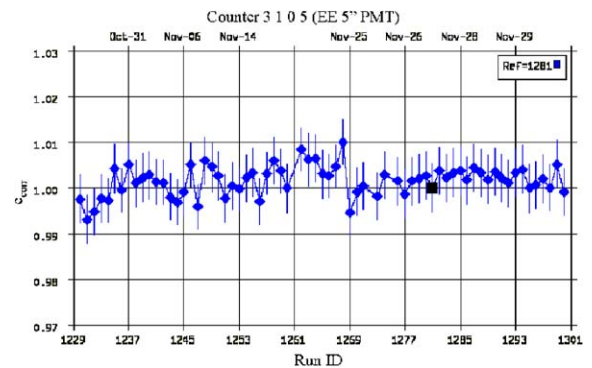


Fig. 30. Sample of the long term (one month) stability for the energy correction parameter  $e_{\text{corr}}$ .

beta decay isotopes, with the detector and the source of the double beta decay being independent. This allows the collaboration to study seven  $\beta\beta$  isotopes simultaneously. The isotopes which are distributed among 20 sectors are  $^{100}\text{Mo}$ ,  $^{82}\text{Se}$ ,  $^{130}\text{Te}$ ,  $^{116}\text{Cd}$ ,  $^{150}\text{Nd}$ ,  $^{96}\text{Zr}$  and  $^{48}\text{Ca}$ . A calorimeter made of large blocks of scintillators coupled to very low radioactivity PMTs permits one to measure the energies of electrons, positrons, gamma-rays and also their time-of-flight, which are used to reject events from external backgrounds. In addition of a tracking volume with delayed tracking electronics for identification of alpha particles coming from  $^{214}\text{Bi}$  decay, a 25 Gauss magnetic field allows three-dimensional track reconstruction of charged particles. Thus the NEMO 3 detector is able to identify electrons, positrons,  $\gamma$ -rays and  $\alpha$ -particles and to detect multi-particle events in the energy domain of natural radioactivity. Using registered events in the  $e^-\gamma$ ,  $e^-\gamma\gamma$ ,  $e^-\gamma\gamma\gamma$  and  $e^-\alpha\gamma$  channels for backgrounds studies, the NEMO 3 detector is able to characterize and measure its own background, which can be subtracted from the two-electron signal.

The main objective of the NEMO 3 experiment is to search for neutrinoless double beta decay. To avoid the high energy region of natural radioactivity the  $\beta\beta 0\nu$  isotopes are selected for their high  $Q_{\beta\beta}$  value. Every attempt has been made to minimize internal backgrounds in the  $\beta\beta 0\nu$  sources by purification of the enriched samples as well to suppress external backgrounds using shields and by carefully selecting all the detector materials. The tail of the  $\beta\beta 2\nu$  decay distribution troublesome overlaps the  $\beta\beta 0\nu$  distribution as a function of the energy resolution. It is the unavoidable background for neutrinoless double beta decay studies.

The NEMO 3 detector has been running in the Fréjus Underground Laboratory in nearly optimal conditions since mid-February 2003. Figs. 31 and 32 reflect the performance of the detector. The first shows the distribution of the summed two electron energies of  $\beta\beta 2\nu$  events measured for the molybdenum sources (background subtracted). The data sample corresponds to 650 h of data for the runs from mid-February to the end of March 2003. The

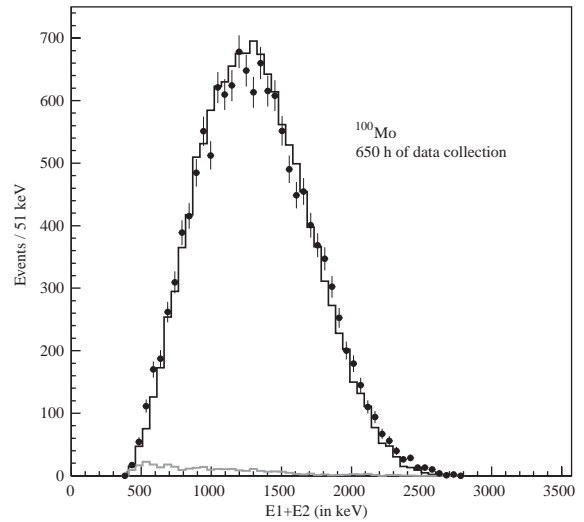


Fig. 31. Distribution of the experimental total energy sum measured with molybdenum sources (with Monte-Carlo computed background subtracted, in grey) compared to  $\beta\beta 2\nu$  Monte-Carlo data. It corresponds to 650 h of data collection in stable conditions, between mid-February and the end of March 2003. The number of events is  $\sim 14000$ , with a signal-to-background ratio of 40 to 1.

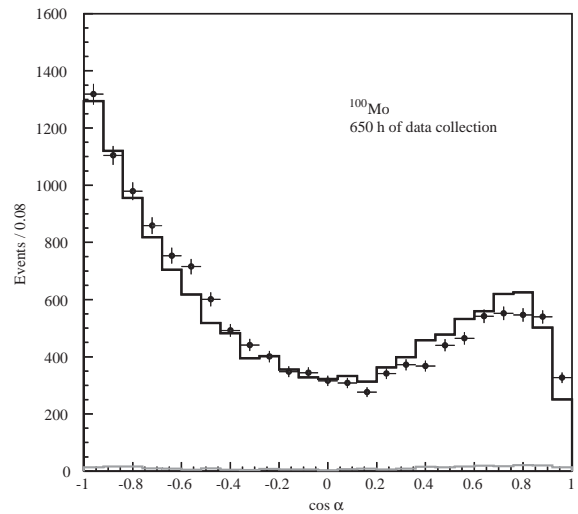


Fig. 32. Experimental angular distribution for molybdenum sources (with Monte Carlo computed background subtracted, in grey) compared to  $\beta\beta 2\nu$  Monte Carlo calculations. The distribution corresponds to the data in Fig. 31.

number of events is 13750, with a signal-to-background ratio of 40:1. The second figure presents the experimental angular distribution for

the two emitted electrons in molybdenum sources (background subtracted). The same data for the summed energy and angular distribution are shown with the  $\beta\beta 2\nu$  Monte Carlo calculation. The high statistics of the data will allow for detailed checks of the models used for the Monte Carlo calculation.

### Acknowledgements

The authors would like to thank the Fréjus Underground Laboratory staff for their technical assistance in building and running the experiment. The portion of this work conducted in Russia for source development was supported by INTAS grant number 00-00362.

### References

- [1] W.H. Furry, Phys. Rev. 56 (1939) 1184.
- [2] A.S. Barabash, Czech. J. Phys. 52 (2002) 567.
- [3] D. Dassié, et al., NEMO collaboration, Nucl. Instr. and Meth. A 309 (1991) 465.
- [4] R. Arnold, et al., NEMO collaboration, Nucl. Instr. and Meth. A 354 (1995) 338.
- [5] NEMO collaboration, NEMO3 Proposal, LAL 94-29, 1994.
- [6] G. Audi, A.H. Wapstra, Nucl. Phys. A 595 (1995) 409.
- [7] R.B. Firestone, V.S. Shirley (Eds.), Table of Isotopes 8th ed., 1996.
- [8] E. Browne, R.B. Firestone, V.S. Shirley (Eds.), Table of Radioactive Isotopes, 1986.
- [9] D. Dassié, et al., NEMO collaboration, Phys. Rev. D 51 (1995) 2090.
- [10] T. Bernatowicz, et al., Phys. Rev. Lett. 69 (1992) 2341.
- [11] N. Takaoka, Y. Motomura, K. Nagao, Phys. Rev. C 47 (1996) 1557.
- [12] R. Arnold, et al., NEMO collaboration, Nucl. Instr. and Meth. A 474 (2001) 93.
- [13] R. Arnold, et al., NEMO collaboration, Nucl. Phys. A 636 (1998) 209.
- [14] R. Arnold, et al., NEMO collaboration, Z. Phys. C 72 (1996) 239.
- [15] R. Arnold, et al., NEMO collaboration, Nucl. Phys. A 658 (1999) 299.
- [16] J. Busto, et al., Nucl. Instr. and Meth. A 492 (2002) 35.
- [17] Y. Perrin, et al., CASCADE: Tool kit for the construction of distributed real time data acquisition systems, Conference Records of RT 93, Vancouver, 1993.
- [18] H. Ohsumi, et al., NEMO collaboration, Nucl. Instr. and Meth. A 482 (2002) 832.
- [19] C. Marquet, et al., NEMO collaboration, Nucl. Instr. and Meth. A 457 (2001) 487.
- [20] R. Arnold, V.I. Tretyak, The NEMO 3 simulation program: current status, CRN 97-01, 1997.
- [21] GEANT - Detector description and simulation tool, CERN Program Library Long Writeup W5013, CERN, 1994.
- [22] EUCLID 3, version 1.1F, Matra Datavision, 1994.
- [23] C. Zeitnitz, T.A. Gabriel, Nucl. Instr. and Meth. A 349 (1994) 106.
- [24] C. Jollet, Ph.D. Thesis, CENBG 02-24, 2002.
- [25] I. Kisel, et al., NEMO collaboration, Nucl. Instr. and Meth. A 387 (1997) 433.
- [26] K. Errahmane, Ph.D. Thesis, LAL 01-20, 2001.
- [27] A.I. Etienvre, Ph.D. Thesis, LAL 03-13, 2003.